Influence of Matrix Strength on Tensile Performance of DFRCC with Bundled Aramid Fiber

(集束型アラミド繊維を用いた DFRCC の引張性能に及ぼすマトリクス強度の影響)

SHI HAOHUI

(Master's Program in Engineering Mechanics and Energy)

Advised by Toshiyuki Kanakubo

Submitted to the Graduate School
of Science and Technology
Degree Programs in Systems and
Information Engineering
in Partial Fulfillment of the Requirements
for the Degree of Master of Engineering
at the University of Tsukuba

March 2022

Abstract

Fiber-Reinforced Cementitious Composite (FRCC) is cementitious material reinforced with short discrete fibers to improve brittle behavior of composite, especially in tensile and bending field. FRCC showing a deflection hardening behavior under bending condition is defined as Ductile Fiber-Reinforced Cementitious Composite (DFRCC). The main advantage of DFRCC is the high tensile performance brought by the bridging effect of fibers across cracks. In order to utilize its advantage in actual structural elements, it is essential to investigate tensile performance of DFRCC according to various factors and develop the evaluation methodologies for it.

This study aims to investigate the influence of matrix strength on the tensile performance of DFRCC with bundled aramid fiber. A total of 45 specimens varying matrix strength and fiber volume fraction were subjected to uniaxial tension test. Most of the DFRCC specimens in tensile failure showed multiple cracks after loading. Number of cracks increased with increasing of matrix strength. Furthermore, the load at first cracking and the maximum load increased with increasing of matrix strength.

By using the pullout characteristic of bundled aramid fiber obtained from previous study, theoretical bridging law was calculated to adapt with the experimental results. According to the calculation, the modified individual fiber pullout model, in which the maximum pullout force is given by the proportional relations with the compressive strength of matrix, could express the uniaxial tension test results well.

In addition, based on the experimental and calculation results, bridging law model, in which feature points were expressed by the function of fiber orientation intensity and matrix strength was proposed. The modeled bridging law was applied to the section analysis for 4-point bending test to verify its adaptability. According to the comparison, the maximum bending moment of experimental results is from 0.910 to 1.105 times of that of analysis results.

Contents

List of Figures

List of Tables

Chapter 1 Introduction

1.1 Research Background

1.1.1 Ductile Fiber-Reinforced Cementitious Composite (DFRCC)

Fiber-Reinforced Cementitious Composite (FRCC) is cementitious material in which short discrete fibers with a certain volume fraction are mixed in mortar matrix to improve brittle behavior of composite especially in tensile and bending field. Compared with traditional mortar matrix, FRCC is expected to have high performance in ductility because of the fiber bridging through cracks which transfers the tensile force as shown in **Figure 1.1(a)**. In addition, FRCC is expected to bring high durability when it is used in Reinforced Concrete (RC) structures because fibers can control the crack openings in matrix which prohibit the penetrations of aggressive attacks to deteriorate the internal reinforced rebars and FRCC itself.

In the past decades, various types of FRCC have been introduced and studied by a number of researchers. As a type in FRCC categories with further improved performance, Ductile Fiber-Reinforced Cementitious Composite (DFRCC) is developed. As a significant characteristic, DFRCC shows a deflection hardening behavior under bending condition which means stress increases after the initial cracks generate [1]. In addition, DFRCC shows multiple cracking behavior which is shown in **Figure 1.1(b)**. The high ductility and durability of DFRCC is achieved by the bridging effect of individual fibers in the mortar matrix.

By applying the high ductility and durability of DFRCC to the structural elements, the reduction of the damage and crack width reduction effect have been reported by a lot of research outcomes (e.g. [2]). Therefore, the application of DFRCC has the potential to bring higher performance (such as: weight saving, high durability) for conventional RC structures and realize structural design for complicated structures.

It has been reported that High Performance Fiber-Reinforced Cement Composite (HPFRCC), which is included in the category of DFRCC and showing strain-hardening behavior under uniaxial tension, has been applied in high-rise housing in crucial parts such as coupling beams [3]. However, there are few examples of applying DFRCC for structural elements expecting its fiber bridging effect. The current condition is that DFRCC is mainly expected for controlling effect of crack openings and prevention effect of peelings, and as a result, it is mainly used for non-structural elements [4].

As one of the main reasons why DFRCC is hardly used for structural elements, a normative evaluation of its tensile performance has not been fully developed. It is extremely difficult to evaluate the tensile performance of DFRCC quantitatively because bond performance of individual fibers with matrix and orientation of fibers in matrix would change due to various factors.

(a) **(b)**

Figure 1.1 DFRCC under bending condition:
(a) Fiber bridging through crack; (b) Multiple cracking behavior

1.1.2 Aramid fibers applied in DFRCC

According to various studies, steel fibers or polymeric fibers such as polyethylene (PE), polyvinyl alcohol (PVA), and polypropylene (PP) fibers have been utilized in FRCC. While FRCC mixing with steel fibers commonly shows tension softening behavior after initial cracking, polymeric fibers are commonly used rather than steel fibers in DFRCC which shows higher ductility.

Aramid fiber is known as one of the polymeric fibers that have high tensile strength, durability, and heat and chemical resistance. It has been reported that aramid fiber has been used for the strengthening for RC structures by the external bonding of a fiber sheet. However, few research studies can be found concerning FRCC mixed with discrete aramid fibers [5-6]. Since a commercially provided single aramid fiber has a small diameter of 12 μm, it cannot be expected that the aramid fibers and the cementitious matrix have a strong bond strength [7]. In the case of PVA fiber, it has been considered that the alcohol group in a PVA molecule leads to the good bond performance with the cementitious matrix. However, as for other types of polymeric fibers, the smooth surface of an individual fiber cannot generate a strong bond resistance.

For these reasons, this study has been focusing on bundled aramid fiber, which is made with a bundling of original yarns of aramid fiber as shown in **Figure 1.2**. Bundled aramid fiber shows a rough surface, and it is expected to have good bond performance with the cementitious matrix by mechanical resistance.

Figure 1.2 Bundling of original yarns of aramid fiber

1.1.3 Evaluation for Tensile Performance of DFRCC (Fiber Bridging Law)

The high tensile performance of FRCC is brought by the bridging effect of fibers across cracks after initial cracking of the matrix. Therefore, fiber bridging stress - crack width relationship called bridging law has been studied by lots of researchers to evaluate tensile performance of FRCC. According to previous studies, bridging law can be obtained experimentally (e.g., from a uniaxial tension test). On the other hand, theoretical solution of bridging law based on micromechanics has been introduced by some researchers.

Since the bridging effect of fibers is strongly influenced by the fiber types and dimensions, the pullout behavior of an individual fiber from cementitious matrix has been investigated, to reflect these factors on bridging law. A number of researchers have conducted pullout tests for various types and dimensions of fibers, e.g., steel fiber [9], bundled aramid fiber [10], nylon and polypropylene (PP) fibers [11].

Bridging law can be obtained by an integral calculus of forces carried by individual bridging fibers, considering the orientation and distribution of fibers in matrix [8]. In order to evaluate the orientation and distribution of fibers in matrix quantitatively, Kanakubo et al. has introduced a probability density function (PDF) for fiber inclination angle and fiber centroidal location expressing by an elliptic function [12].

Bridging laws for PVA-FRCC [13] and bundled aramid-FRCC [10] have also introduced by Kanakubo et al. From the results, both calculated bridging laws showed good agreements with the results of uniaxial tension test. In addition, the calculated bridging laws have been simply modeled by several researchers, e.g., tri-linear model for PVA-FRCC [14], bi-linear model for bundled aramid-FRCC [15]. These models make it possible to evaluate the bridging effect in various types of FRCC members approximately.

1.2 Research Objective

In recent years, requirements for concrete structures have diversified and advanced. Consequently, the performance required for RC structures is also increasing. In addition, it is considered that the importance of extending the life cycle of structures, which improves global environment problems, would be further enhanced in the future. For such social requirements, DFRCC would be useful and has the potential to solve various tasks when applying to structural elements. Therefore, it is essential to investigate the mechanical performance especially tensile performance of DFRCC according to various factors and develop the evaluation methodologies for its mechanical performance.

In the past decades, a number of researchers have investigated the tensile performance of FRCC via several factors. Li et al. [16] and Park et al. [17] has introduced the tensile performance of Ultra-High-Performance Concrete (UHPC) with different hybrid fibers. Kanakubo et al. has investigated the influence of fiber orientation on bridging performance of PVA-FRCC [12]. However, it can be seen that the research studies on mechanical performance of FRCC categories mainly focused on the influence of fibers (e.g., types, adding amount, orientation), while few research studies could be found considering the influence of mortar matrix.

According to this situation, this study focuses on the property of mortar matrix applied in DFRCC. The main objective of this study is to investigate the influence of matrix strength on the tensile performance of DFRCC with bundled aramid fiber. In this study, matrix strength and fiber volume fraction are considered as main parameters. Uniaxial tension test was conducted for DFRCC rectangular prism specimens with slits to find out the relationship between tensile performance and the two parameters.

In addition, by using the pullout characteristic of bundled aramid fiber obtained from previous study [10], theoretical bridging law was calculated to adapt with the experimental results. The calculated bridging law was simplified to a bilinear model, in which feature points are expressed by the function of fiber orientation intensity and matrix strength. After that, the modeled bridging law was applied to the section analysis under bending condition. Comparison between analysis results and experimental results obtained from 4-point bending test was discussed to verify the adaptability of modeled bridging law.

Chapter 2 Uniaxial Tension Test

2.1 Introduction

In this chapter, the uniaxial tension test is conducted for DFRCC rectangular prism specimens with slits using bundled aramid fibers to investigate the influence of matrix strength on tensile performance. The tensile performance is compared to each other through the load P – total crack width w relationships obtained from the experiment. Furthermore, the crack pattern and fibers on the fracture surface are observed and discussed.

2.2 Experiment Outline

2.2.1 Specimens

List of specimens are shown in **Table 2.1**. Matrix strength and fiber volume fraction are considered as main experimental parameters in this study. The target compressive strength of the mortar matrix was set to 24MPa, 36MPa, and 48MPa for Fc24, Fc36, and Fc48 series of specimens, respectively. Fiber volume fraction was varied as none (mortar), 1%, 2% for each matrix strength. Therefore, 9 series of specimens were determined for uniaxial tension test.

Figure 2.1 shows the dimension of specimen for uniaxial tension test. Specimen is DFRCC rectangular prism with two bolts (M20) embedded at both ends to transfer the tensile load. In order to control the position of crack opening, two slits were set on both narrow sides in the middle of specimen. For each series, five specimens were manufactured and tested.

Table 2.1 List of specimens

Series	No.	Target matrix strength [MPa]	Fiber volume fraction [%]
Fc24-N	1-5	24	None
Fc24-1%	1-5		1
Fc24-2%	1-5		2
Fc36-N	1-5	36	None
Fc36-1%	1-5		1
Fc36-2%	1-5		2
Fc48-N	1-5	48	None
Fc48-1%	1-5		1
Fc48-2%	1-5		2

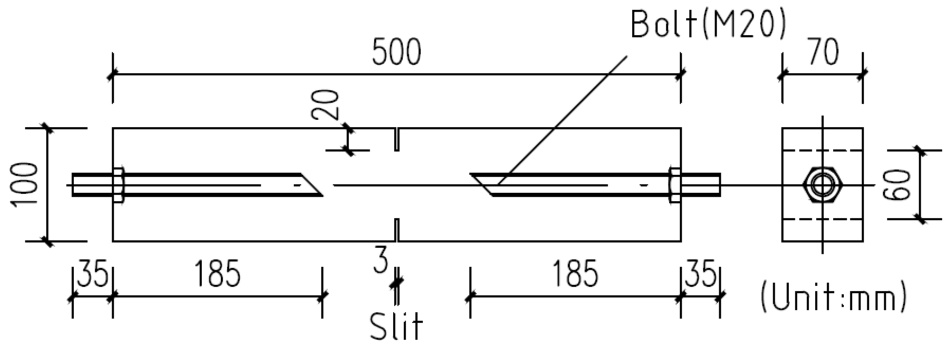

Figure 2.1 Dimension of specimen for uniaxial tension test

2.2.2 Applied Materials

The aramid fiber applied in this study is a bundled fiber. The original yarns of aramid fibers with a nominal diameter of 12μm are twisted to form a thick individual fiber and sized not to unravel in FRCC. **Table 2.2** shows the dimension and mechanical properties of fiber applied in this study and **Figure 2.2** shows its visual appearance. The unit weight of bundled aramid fibers mixed in DFRCC for volume fraction of 1% and 2% is 13.9kg/m^3 and 27.8kg/m^3, respectively.

Table 2.3 shows the three mix proportions of cementitious matrix applied in this study. Materials in the three mix proportions are different in the ratio of cement to fly ash to obtain different target compressive strength. Since the fresh DFRCC shows self-consolidating property, fresh DFRCC was poured from one end of the mold and allowed to flow naturally until the mold was full filled. The specimens were cured in the natural environment.

Table 2.2 Dimension and mechanical properties of fiber

Fiber type	Length [mm]	Diameter [mm]	Tensile strength [MPa]	Elastic modulus [GPa]
Bundled aramid fiber	30	0.50	3432*	73*

* Properties obtained from original yarns

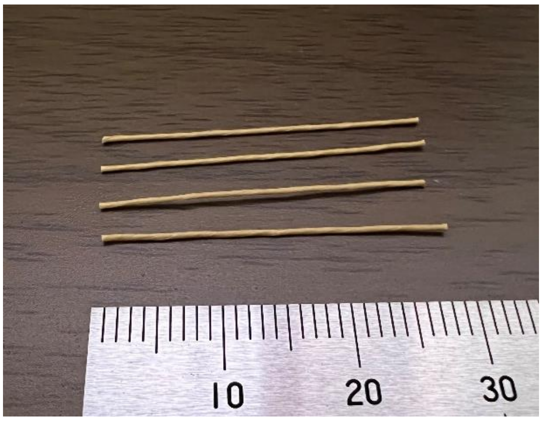

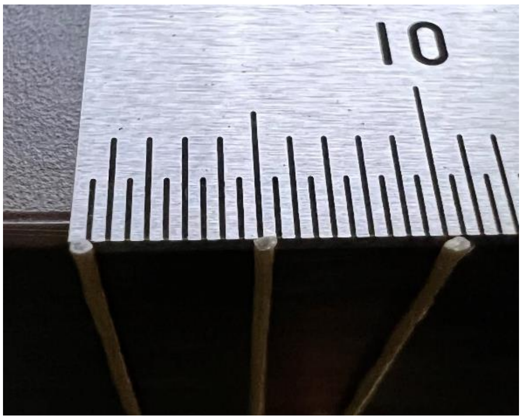

(a) **(b)**

Figure 2.2 Visual appearance of bundled aramid fiber: (a) Length; (b) Diameter

Table 2.3 Mix proportions of cementitious matrix

Series	W/C	W/B	FA/B	Unit weight [kg/m^3]						
				W	C	FA	S	SP	TH	SR
Fc24	0.785	0.392	0.500	380	484	484	484	6	2	9.68
Fc36	0.560	0.392	0.300	380	678	291	484	6	2	13.56
Fc48	0.436	0.392	0.100	380	872	97	484	6	2	17.44

where,

B = binder (= C + FA),
W = water,
C = cement (High early strength Portland cement),
FA = fly ash (Type II of Japanese Industrial Standard (JIS A 6202)),
S = sand (size under 0.2 mm),
SP = high-range water-reducing agent (= B × 0.6%),
TH = thickener,
SR = shrinkage reducing agent (= C × 2%).

2.2.3 Loading and Measurement

Uniaxial tension test was conducted using a universal testing machine with the capacity of 2MN. **Figure2.3** shows the setup of the loading and measurement for uniaxial tension test. Since the increasing external moment caused by setup irregularity and local fracture caused by secondary moment would be an inevitable factor to the experiment, pin-fix ends were applied at the boundaries to minimize possible effects to the results. Two displacement transducers (Pi-type) were set at the middle area of 100mm in length on both sides to measure the crack width at the slit position. The loading speed was set to be 0.5-1mm/min as the head speed. Visible cracks observation and photographing were done after loading. In addition, the upper and lower parts of the specimen were forcibly pulled apart and fibers on the fracture surface were counted.

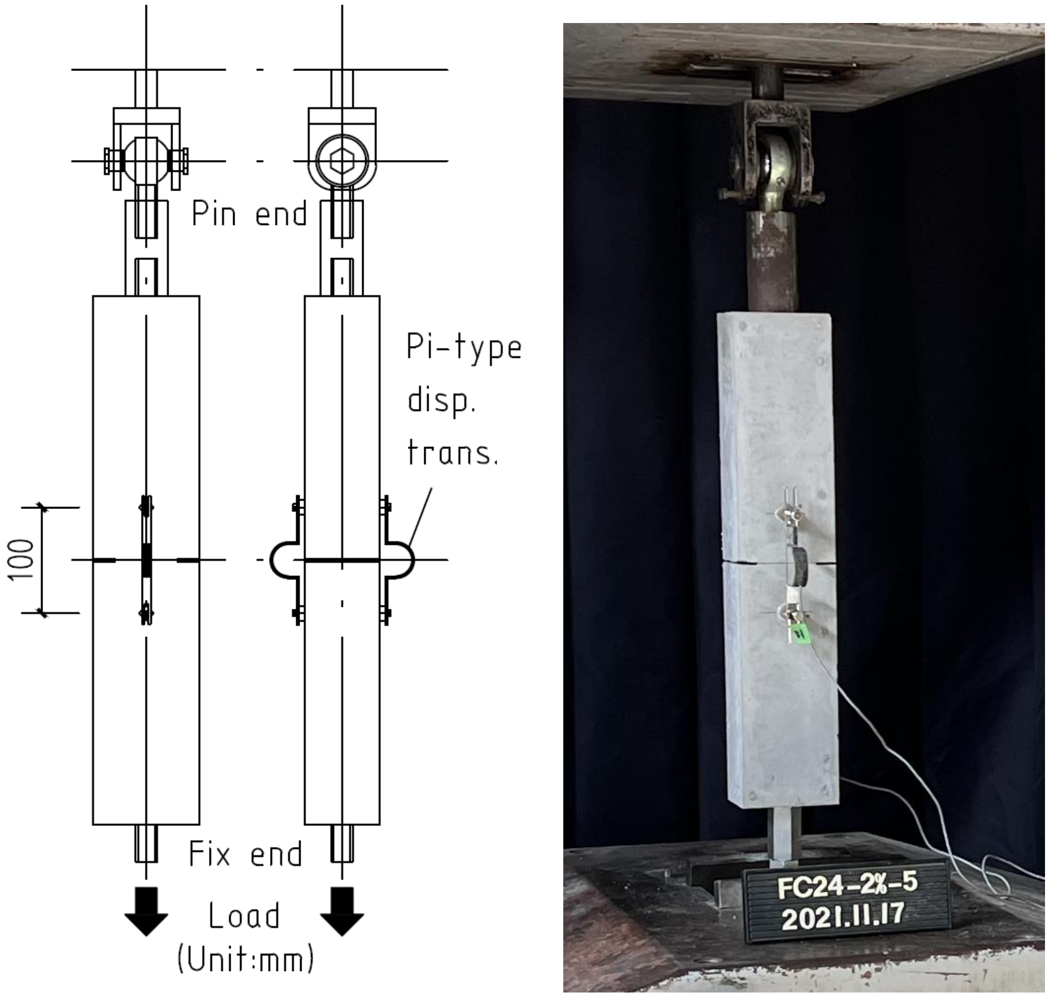

Figure 2.3 Setup of loading and measurement for uniaxial tension test

2.3 Experiment Results

2.3.1 Compressive Properties

Before uniaxial tension test, compressive test was conducted to confirm the compressive strength and elastic modulus. For each series, three cylinder specimens ($\varphi100 \times 200$mm) were tested. **Table 2.4** lists the compressive properties of each series. As shown by the results, the exact compressive strength was much stronger than the target compressive strength. Compressive strength of the three mix proportions showed obvious difference to each other. In addition, compressive strength decreased when fibers were mixed into the matrix.

Table 2.4 Compressive properties (Uniaxial tension test)

Series	Fiber volume fraction [%]	Curing time [Days]	Compressive strength [MPa]	Elastic modulus [GPa]
Fc24	None	25	38.3	14.2
	1		35.6	13.6
	2		33.3	13.0
Fc36	None	32	54.6	18.2
	1		48.2	17.8
	2		46.1	17.6
Fc48	None	45	71.4	20.0
	1		66.9	19.7
	2		63.7	19.3

2.3.2 Failure Mode under Tension

Figure 2.4 shows the failure modes of specimen under tension. Failure modes of specimens can be mainly divided into two types: tensile failure and bending failure. The specimens of tensile failure generated one obvious crack throughout the slits on both sides. The specimens of bending failure generated a slanting crack from one slit, and it did not penetrate to the slit at the other side. The occur of bending failure is considered to be caused by the nonuniform distribution of the fibers in the matrix. The specimens, in which failure mode was detected to be bending failure, are not discussed in the following parts.

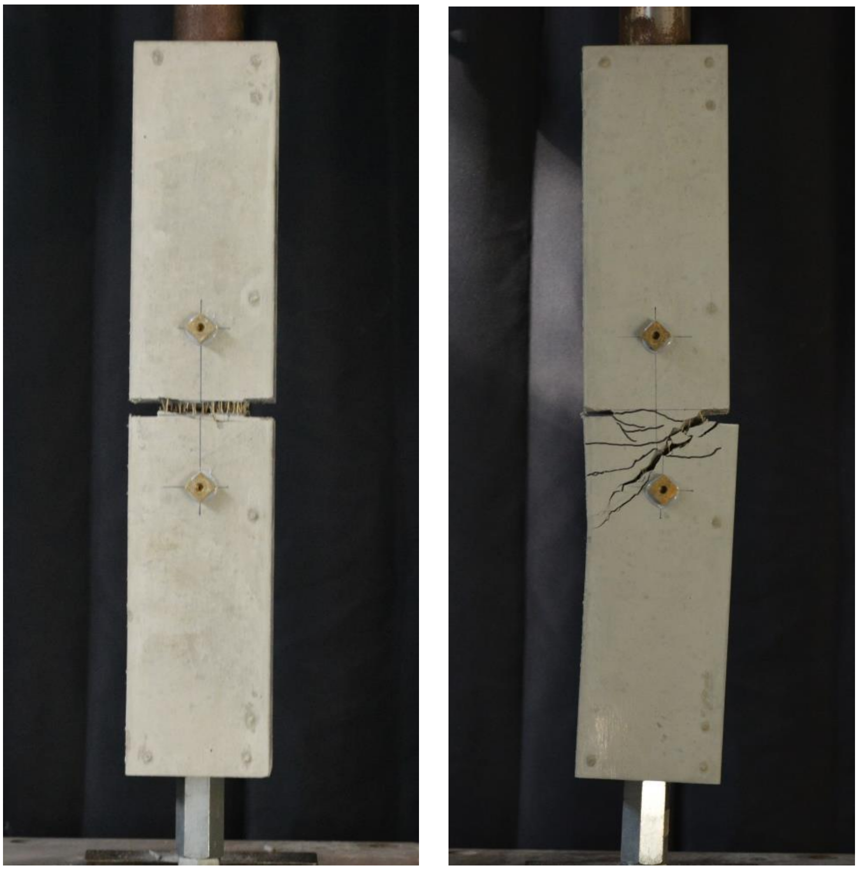

(a) (b)

Figure 2.4 Failure modes of specimen under tension:
(a) Tensile failure; (b) Bending failure

2.3.3 Crack Pattern and Crack Width

Figure 2.5 shows the examples of crack pattern of specimens in tensile failure. As revealed by the figure, specimens without fibers (mortar) only generated one crack throughout the slits. As for DFRCC specimens, an obvious crack throughout slits could be observed while multiple fine cracks generated near the slits. **Table 2.5** shows the number of cracks in testing area for each specimen. As for DFRCC series, average number of cracks increased with increasing of fiber volume fraction and matrix strength.

In the gauge length of 100mm, the total crack width w was obtained by averaging the two values (w_1, w_2) measured by the two displacement transducers (Pi-type) on both sides of specimen ignoring the elastic deformation of mortar matrix.

	N (Mortar)	1%	2%
Fc24	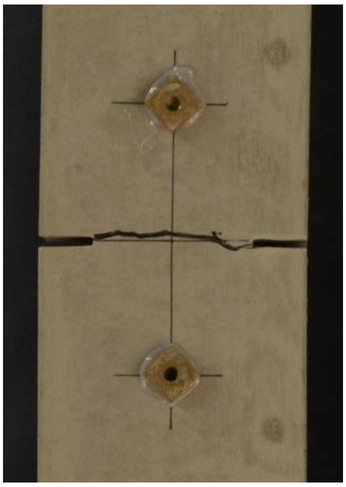		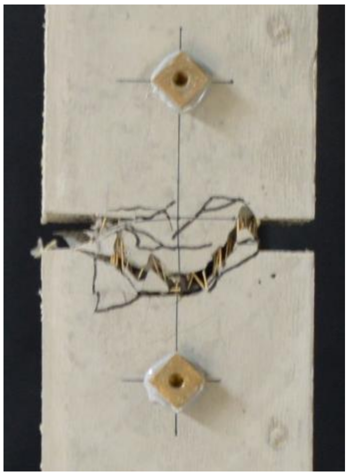
Fc36	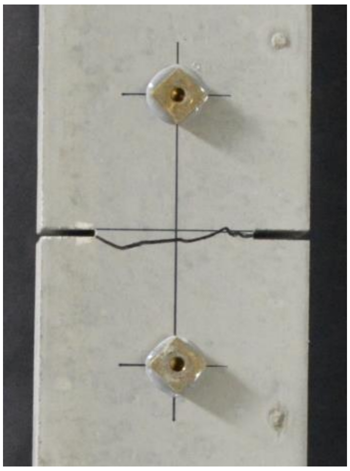	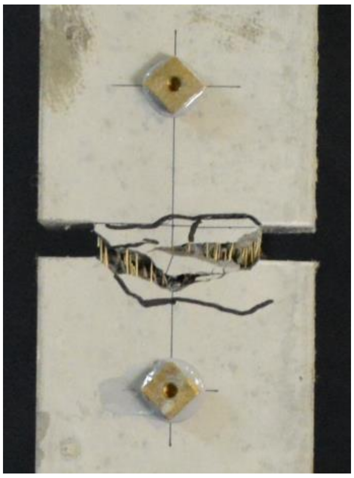	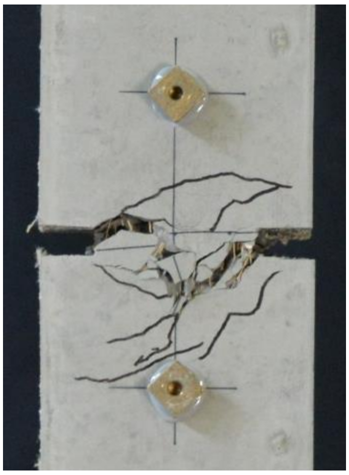
Fc48	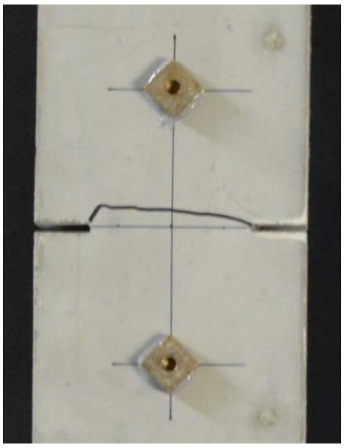	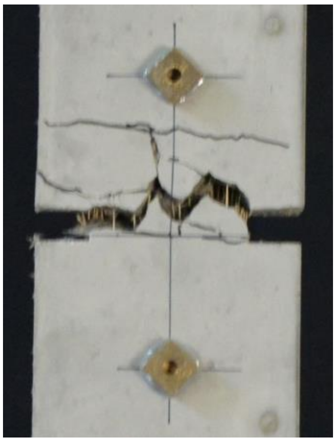	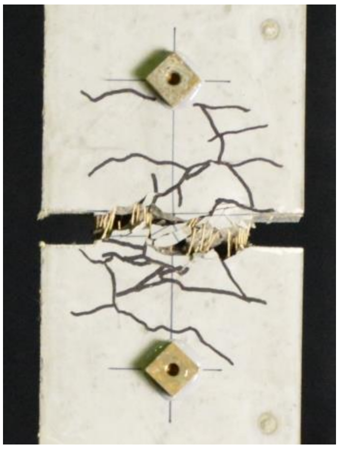

Figure 2.5 Examples of crack pattern (tensile failure)

Table 2.5 Number of cracks in testing area

Specimen		Number of cracks			Average number of cracks for each series
Series	No.	Front side	Back side	Average	
Fc24-N	1	1	1	1.0	1.0
	2	1	1	1.0	
Fc24-1%	1	2	2	2.0	1.6
	2	3	2	2.5	
	3	1	2	1.5	
	4	1	1	1.0	
	5	1	1	1.0	
Fc24-2%	2	3	3	3.0	3.2
	3	4	3	3.5	
	4	3	3	3.0	
Fc36-N	1	1	1	1.0	1.0
	2	1	1	1.0	
	3	1	1	1.0	
Fc36-1%	1	1	3	2.0	3.1
	2	3	2	2.5	
	3	5	4	4.5	
	4	3	3	3.0	
	5	3	4	3.5	
Fc36-2%	4	4	3	3.5	3.5
Fc48-N	2	1	1	1.0	1.0
	3	1	1	1.0	
	4	1	1	1.0	
Fc48-1%	1	4	5	4.5	3.5
	2	3	4	3.5	
	3	3	2	2.5	
	4	4	4	4.0	
	5	3	3	3.0	
Fc48-2%	2	6	4	5.0	4.7
	3	5	5	5.0	
	4	4	4	4.0	

2.3.4 Load *P* - Crack width *w* Relationship

Figure 2.6 shows the load P - total crack width w relationship obtained from uniaxial tension test. In order to compare the tensile performance between each series, the average curve of test results in each series is also shown in **Figure 2.6** as red line. In the case of specimens without fibers (mortar), load decreased instantaneously to 0 when first crack generated. As for DFRCC specimens, load decreased gradually after peak to a wide crack width. In addition, DFRCC specimens showed a tensile strain-hardening property that load increases after the crack generated.

Table 2.6 shows the load at first crack P_1 and crack width at first crack w_1 for each specimen. **Figure 2.7** shows the relationship between the load at first crack P_1 and matrix strength f_c. The lines in **Figure 2.7** are connected by the average values of the load at first crack P_1 in each series. As revealed by the results, the load at first crack P_1 of DFRCC specimens is larger than that of specimens without fibers (mortar), indicating that the addition of fibers has an inhibitory effect on crack occurring. The load at first crack P_1 increased with increasing of fiber volume fraction and matrix strength.

Table 2.7 shows the maximum load P_{max} and total crack width at maximum load w_{max} for each specimen. **Figure 2.8** shows relationship between the maximum load P_{max} and matrix strength f_c. The lines in **Figure 2.8** are connected by the average values of the maximum load P_{max} in each series. As revealed by the results, the maximum load P_{max} of DFRCC specimens is larger than the load at first crack P_1, which confirms a tensile strain-hardening property. By comparing the specimens with the same fiber volume fraction, average maximum load $P_{max.a}$ increased as increasing of matrix strength. On the other hand, by comparing the specimens with the same mix proportion of mortar matrix, average maximum load $P_{max.a}$ increased as increasing of fiber volume fraction.

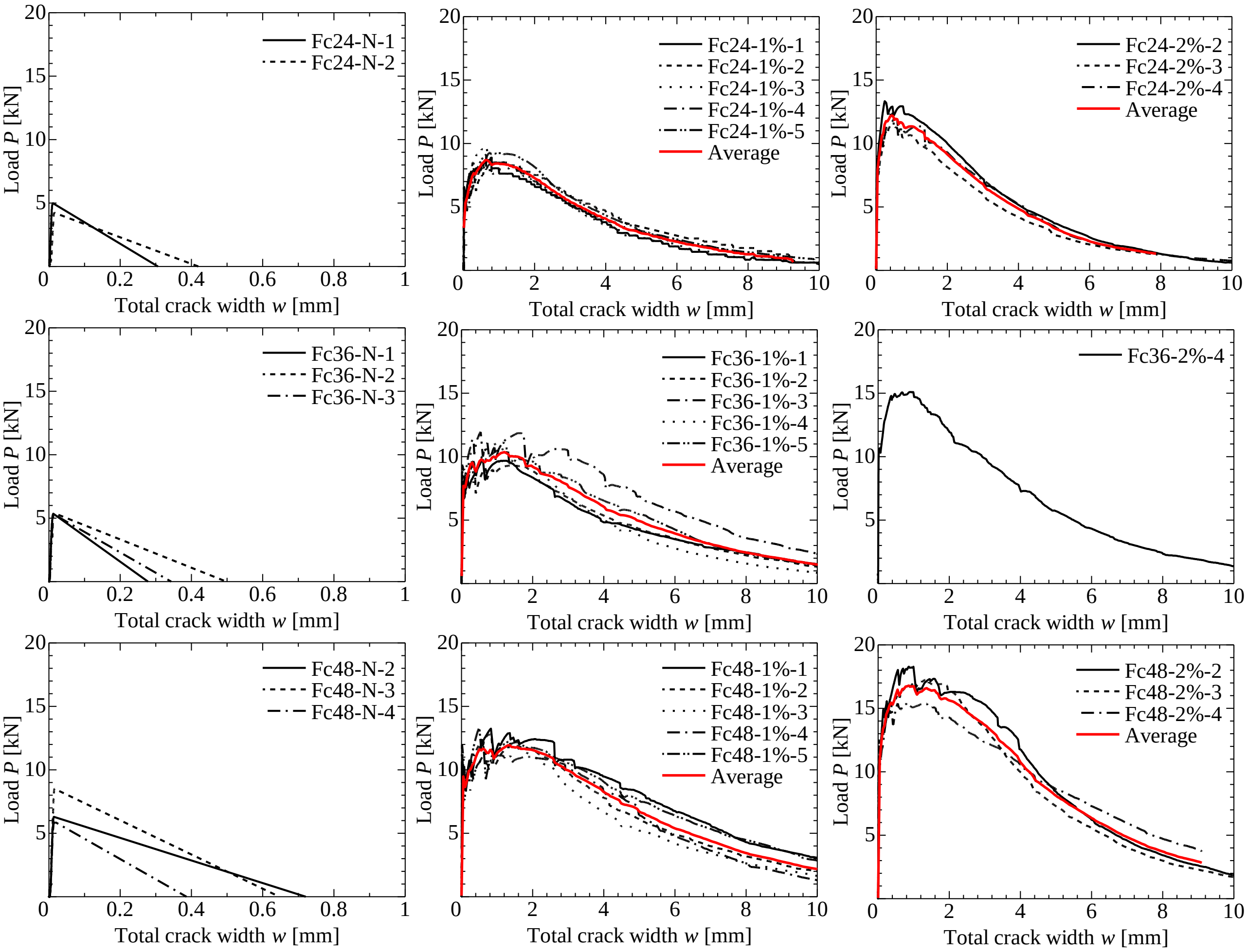

Figure 2.6 Load P – total crack width w relationship

Table 2.6 Load at first crack P_1 and crack width at first crack w_1

Specimen		Load at first crack	Crack width at first crack	Average load at first crack
Series	No.	P_1 [kN]	w_1 [mm]	$P_{1.a}$ [kN]
Fc24-N	1	4.99	0.011	4.61
	2	4.24	0.015	
Fc24-1%	1	6.57	0.022	6.03
	2	5.23	0.028	
	3	6.58	0.013	
	4	6.37	0.027	
	5	5.38	0.025	
Fc24-2%	2	8.66	0.026	7.87
	3	7.54	0.019	
	4	7.40	0.024	
Fc36-N	1	5.35	0.013	5.35
	2	5.40	0.014	
	3	5.30	0.014	
Fc36-1%	1	7.51	0.014	8.36
	2	9.53	0.023	
	3	8.10	0.020	
	4	7.69	0.023	
	5	8.94	0.017	
Fc36-2%	4	10.34	0.018	10.34
Fc48-N	2	6.30	0.014	6.89
	3	8.51	0.016	
	4	5.87	0.019	
Fc48-1%	1	11.03	0.020	10.29
	2	9.20	0.020	
	3	11.54	0.017	
	4	11.97	0.017	
	5	7.71	0.016	
Fc48-2%	2	10.71	0.018	11.27
	3	12.54	0.019	
	4	10.55	0.014	

Table 2.7 Maximum load P_{max} and total crack width at maximum load w_{max}

Specimen Series	Specimen No.	Maximum load P_{max} [kN]	Total crack width at maximum load w_{max} [mm]	Average maximum load $P_{max.a}$ [kN]
Fc24-N	1	4.99	0.011	4.61
	2	4.24	0.015	
Fc24-1%	1	8.88	0.780	8.99
	2	8.54	1.106	
	3	9.76	0.627	
	4	8.49	1.100	
	5	9.28	0.750	
Fc24-2%	2	13.33	0.241	12.60
	3	12.05	0.559	
	4	12.41	0.466	
Fc36-N	1	5.35	0.013	5.35
	2	5.40	0.014	
	3	5.30	0.014	
Fc36-1%	1	9.75	0.604	10.62
	2	9.53	0.023	
	3	11.95	0.539	
	4	11.21	1.109	
	5	10.65	1.230	
Fc36-2%	4	15.10	0.927	15.10
Fc48-N	2	6.30	0.014	6.89
	3	8.51	0.016	
	4	5.87	0.019	
Fc48-1%	1	13.25	0.828	12.63
	2	12.82	0.824	
	3	11.80	1.275	
	4	11.97	0.017	
	5	13.33	0.500	
Fc48-2%	2	18.28	0.865	17.03
	3	17.27	1.391	
	4	15.53	0.327	

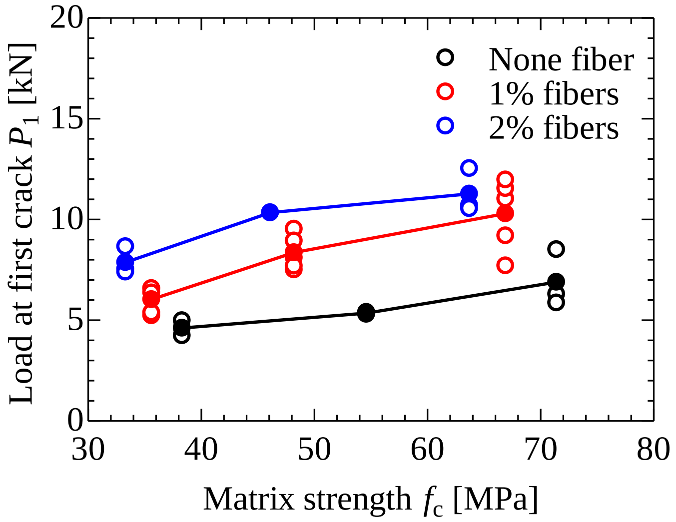

Figure 2.7 Relationship between load at first crack P_1 and matrix strength f_c

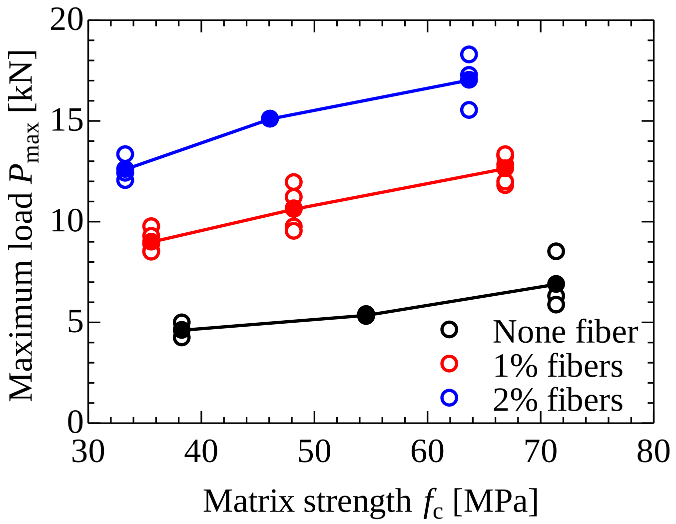

Figure 2.8 Relationship between maximum load P_{max} and matrix strength f_c

2.3.5 Fibers on Fracture Surface

Figure 2.9 shows the examples of the visual appearance of fracture surface in Fc36 series. It could be detected that several fibers on the fracture surface unraveled when they were pulled out from the mortar matrix. However, it is difficult to confirm whether the fibers ruptured or not due to tensile stress by visible observation.

Table 2.8 shows the number of fibers on fracture surface for each specimen counted after loading. As revealed by the results, the specimen with a larger number of fibers showed a higher maximum load P_{max}. However, the average number of fibers on the fracture surface was not proportional as expected. Although the measured amount of fibers was added at the mixture, inconstant fiber distribution could be observed in the case of relatively small dimensions of specimen.

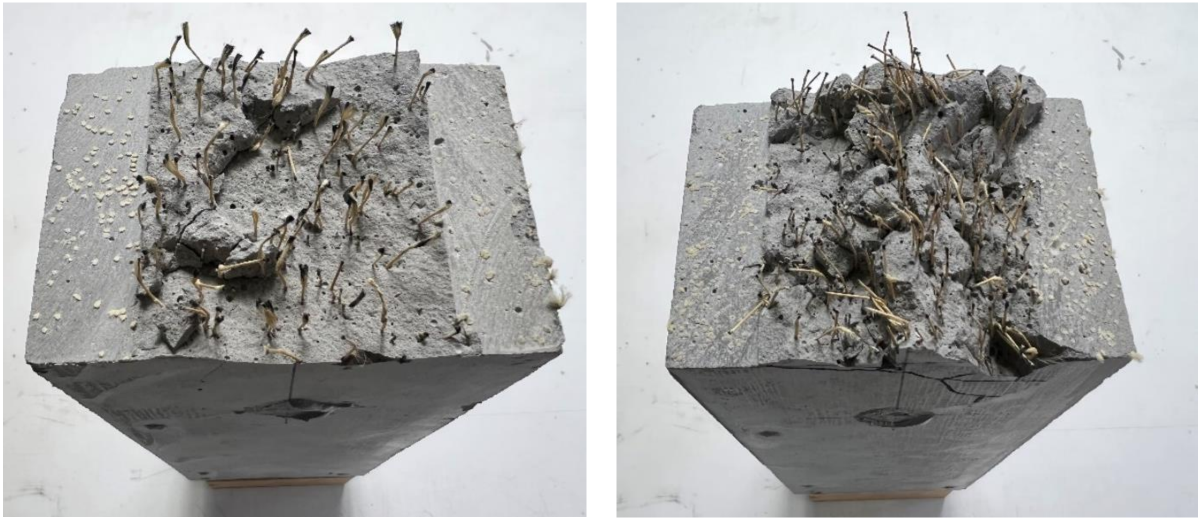

(a) (b)

Figure 2.9 Examples of the visual appearance of fracture surface (Fc36)
(a) Fiber volume fraction: 1%; (b) Fiber volume fraction: 2%

Table 2.8 Number of fibers on fracture surface

Specimen		Maximum load	Number of fibers			Average number of fibers
Series	No.	P_{max} [kN]	Top side	Bottom side	Total	
Fc24-1%	1	8.88	99	106	205	205.6
	2	8.54	90	108	198	
	3	9.76	109	112	221	
	4	8.49	95	97	192	
	5	9.28	103	109	212	
Fc24-2%	2	13.33	182	151	333	313.3
	3	12.05	159	145	304	
	4	12.41	174	129	303	
Fc36-1%	1	9.75	96	82	178	193.8
	2	9.53	89	79	168	
	3	11.95	118	109	227	
	4	11.21	107	93	200	
	5	10.65	101	95	196	
Fc36-2%	4	15.10	163	152	315	315.0
Fc48-1%	1	13.25	101	97	198	195.8
	2	12.82	105	86	191	
	3	11.80	92	94	186	
	4	11.97	97	101	198	
	5	13.33	107	99	206	
Fc48-2%	2	18.28	156	148	304	297.0
	3	17.27	163	144	307	
	4	15.53	131	149	280	

Chapter 3 Calculation of Bridging Law and Modeling

3.1 Introduction

In this chapter, theoretical bridging law is calculated based on the pullout characteristic of bundled aramid fiber obtained from previous study [10]. A coefficient α is introduced in the calculation parameters to reflect the influence of matrix strength on bridging law. Coefficient α is varied to adapt the calculation results with the experimental ones. The calculated bridging law is simplified to a bilinear model, in which feature points are expressed by the function of fiber orientation intensity k and matrix strength f_c. After that, the modeled bridging law is applied to section analysis under bending condition. The analyzed bending moment M - curvature φ relationships are compared with the results obtained from 4-point bending test to verify the adaptability of modeled bridging law.

3.2 Calculation of Bridging Law

3.2.1 Calculation Method

The bridging law (bridging stress σ_{bridge} - crack width w relationship) is calculated by the method proposed in previous study [10]. The bridging law can be obtained by the summation of forces carried by individual bridging fibers considering the probability density function (PDF) for the fiber inclination angle and the fiber centroidal location as given in Equation (1).

$$\sigma_{bridge} = \frac{P_{bridge}}{A_m} = \frac{V_f}{A_f} \cdot \sum_h \sum_j \sum_i P_{ij}\left(w,\psi\right) \cdot p_{xy}\left(\theta_i\right) \cdot p_{zx}\left(\phi_j\right) \cdot p_x\left(y_h, z_h\right) \cdot \Delta\theta \cdot \Delta\phi \cdot \left(\Delta y \cdot \Delta z\right) \quad (1)$$

where,

σ_{bridge} = bridging stress,
P_{bridge} = bridging force (= total of pullout load),
A_m = cross-sectional area of matrix,
V_f = fiber volume fraction,
A_f = cross-sectional area of an individual fiber,
$P(w,\psi)$ = pullout load of an individual fiber,
p_{xy}, p_{zx} = probability density function for fiber inclination angle,
p_x = probability density function for fiber centroidal location,
ψ = fiber inclination angle to x-axis (= max{θ, ϕ}),
θ = angle between x-axis and projected line of the fiber to x-y plane,
ϕ = angle between x-axis and projected line of the fiber to z-x plane,
w = crack width.

The bilinear model proposed in previous study [10] is adapted for the pullout load of an individual fiber, $P(w,\psi)$. The elliptic distribution [12] is adopted for the probability density function (PDF), p_{xy} and p_{zx}, for fiber inclination angles. The elliptic distribution is defined by two parameters: principal orientation angle θ_r (argument of one radius of elliptic function), and orientation intensity k (ratio of the two radii of elliptic function). The fiber orientation in mortar matrix can be expressed by these 2 parameters. The random orientation is given by k = 1. When the value of k is larger than 1, fibers tend to orient towards θ_r. On the other hand, when the value of k is smaller than 1, fibers tend to orient perpendicular to θ_r. The PDF for fiber centroidal location p_x is set to be constant, which means the fibers are randomly distributed along the longitudinal direction of the specimen.

The bridging stress calculated in this method do not include the tensile stress carried by the matrix before cracking. In other words, the calculated bridging law exhibit the tensile stress due to only bridging force of fibers.

3.2.2 Calculation Parameters

Table 3.1 shows the parameters for the calculation of bridging law. The calculation is conducted using a bilinear model for pullout load - crack width relationship of an individual fiber proposed in previous study [10]. In addition, inclined fiber angle and rupture of fiber are also considered in the calculation. The orientation intensity k in the elliptic distribution for the PDF of the fiber inclination angel is set to be 1.5 and 6 for the two planes parallel to the axial direction, which refers to previous study [12]. Furthermore, the principal orientation angle θ_r is set to be 0.

In the bilinear model of pullout behavior of an individual fiber, a coefficient α is introduced in the formula of the maximum pullout load P_{max} to reflect the influence of matrix strength. In the calculation of bridging law, coefficient α is varied to adapt the calculation results with the experimental results.

Table 3.1 Parameters for the calculation of bridging law

Parameter		Input
Cross-sectional area of an individual fiber A_f [mm^2]		0.196
Length of fiber l_f [mm]		30
Apparent rupture strength of fiber σ_{fu} [MPa]		$\sigma_{fu} = 1080 \cdot e^{-0.667\psi}$
Bilinear model	Maximum pullout load P_{max} [N]	$P_{max} = \alpha \cdot l_b$
	Crack width at P_{max} w_{max} [mm]	$w_{max} = 0.13 \cdot l_b^{0.64}$
Elliptic distribution	Orientation intensity for x-y plane k_{xy}	1.5
	Orientation intensity for z-x plane k_{zx}	6
	Principle orientation angle θ_r [deg.]	0

where,

ψ = fiber inclination angle to x-axis [rad.],

l_b = embedded length of fiber [mm],

α = coefficient reflecting the influence of matrix strength.

3.2.3 Calculation Results

From Section **2.3.5**, the number of fibers on fracture surface was not observed to be proportional as expected. In addition, the maximum loads P_{max} in each series showed dispersion. In order to compare with the calculated bridging law, the tensile load P is divided by the total number of fibers of each specimen to express the average tensile force carried by an individual fiber. In the case of calculated bridging law, the tensile load (= P_{bridge}) is divided by the theoretical fiber number across the crack, which can be calculated by $V_f \cdot A_m / A_f \cdot \eta_f$, where η_f, is the fiber effectiveness [12] at the crack width of 0. When the orientation intensity k_{xy} and k_{zx} is 1.5 and 6 respectively, the fiber effectiveness η_f is 0.544.

According to Section **2.3.3**, multiple cracks were detected in the gauge length of the displacement transducers. Since the calculation of bridging law is performed on the fibers through only one cracking surface, in order to compare the experimental results with the calculation ones, the experimental total crack width w is corrected to be regarded as crack width through one crack. The experimental value of total crack width w up to the last peak of the curves is divided by the average number of cracks to obtain a corrected crack width through one crack. The average number of cracks in the gauge length for each specimen is obtained from Section **2.3.3**. After the last peak, the crack opening is considered to be concentrated in one crack, so the post-peak branch of the curves is considering to be the same as the experimental results.

Table 3.2 shows the maximum load per an individual fiber $P_{ind.max}$ for each specimen and calculation result. **Figure 3.1** shows the tensile load per fiber $P_{ind.}$ - crack width w relationship, in which black lines are the corrected experimental results, while red lines are the calculation results. As revealed by the results, the softening branch of the calculated bridging law shows good agreement with the experimental results.

As mentioned in Section **3.2.2**, the coefficient α, which reflects the influence of matrix strength, is varied to adapt the calculation results with the experimental ones. Each series of specimens corresponds to a coefficient α, which is shown in **Table 3.2** and **Figure 3.1**. Linked with the matrix strength f_c shown in section **2.3.1**, **Figure 3.2** shows the relationship between coefficient α and matrix strength f_c. The black lines in **Figure 3.2** exhibit the modified regression calculation results by the least square method, to simplify the relational expression between coefficient α and matrix strength f_c, as given by Equation (2).

$$\alpha = 0.16 \cdot f_c \tag{2}$$

where,

unit for matrix strength f_c is MPa.

Table 3.2 (i) Maximum load per an individual fiber $P_{ind.max}$ (Fc24)

Specimen		Maximum load	Number of fibers			Maximum load per
Series	No.	P_{max} [kN]	Top side	Bottom side	Total	fiber $P_{ind.max}$ [N]
Fc24-1%	1	8.88	99	106	205	43.33
	2	8.54	90	108	198	43.13
	3	9.76	109	112	221	44.15
	4	8.49	95	97	192	44.23
	5	9.28	103	109	212	43.76
Fc24-1% (α=6.0)	Cal.	5.03	$=V_f \cdot A_m / A_f \cdot \eta_f$ $=0.01\times(60\times70)/0.196\times0.544$		116.6	43.23
Fc24-2%	2	13.33	182	151	333	40.04
	3	12.05	159	145	304	39.63
	4	12.41	174	129	303	40.96
Fc24-2% (α=5.5)	Cal.	9.29	$=V_f \cdot A_m / A_f \cdot \eta_f$ $=0.02\times(60\times70)/0.196\times0.544$		233.1	39.91

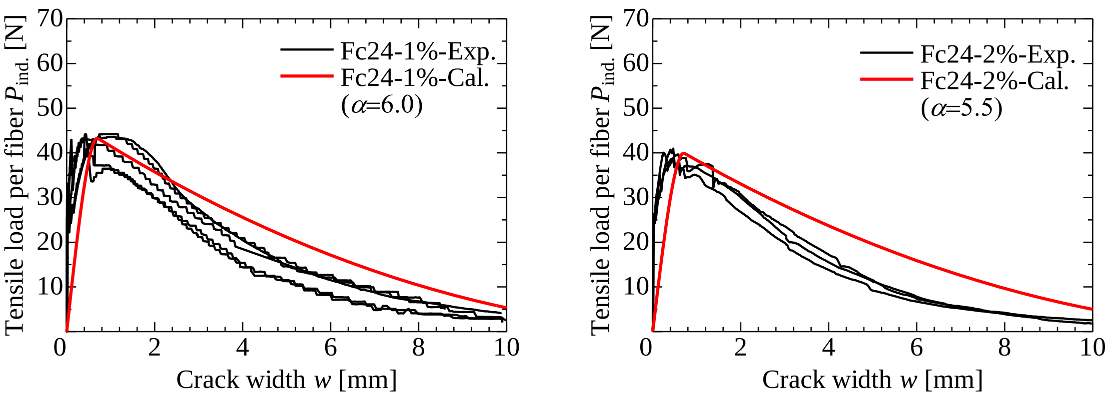

Figure 3.1 (i) Tensile load per fiber $P_{ind.}$ - crack width w relationship (Fc24)

Table 3.2 (ii) Maximum load per an individual fiber $P_{ind.max}$ (Fc36)

Specimen		Maximum load	Number of fibers			Maximum load per
Series	No.	P_{max} (kN)	Top side	Bottom side	Total	fiber $P_{ind.max}$ [N]
Fc36-1%	1	9.75	96	82	178	54.76
	2	9.53	89	79	168	56.73
	3	11.95	118	109	227	52.63
	4	11.21	107	93	200	56.07
	5	10.65	101	95	196	54.33
Fc36-1% (α=8.2)	Cal.	6.31	$=V_f \cdot A_m / A_f \cdot \eta_f$ $=0.01\times(60\times70)/0.196\times0.544$		116.6	54.22
Fc36-2%	4	15.10	163	152	315	47.92
Fc36-2% (α=6.8)	Cal.	11.15	$=V_f \cdot A_m / A_f \cdot \eta_f$ $=0.02\times(60\times70)/0.196\times0.544$		233.1	47.92

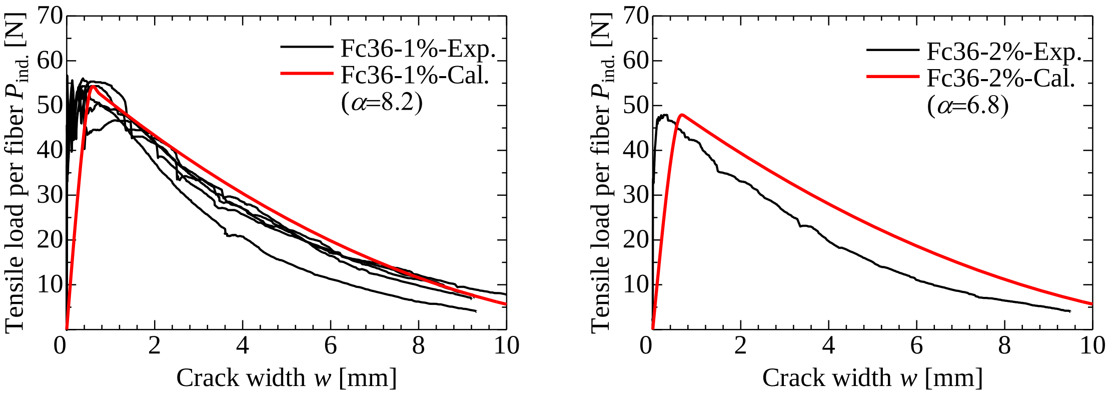

Figure 3.1 (ii) Tensile load per fiber $P_{ind.}$ - crack width w relationship (Fc36)

Table 3.2 (iii) Maximum load per an individual fiber $P_{ind.max}$ (Fc48)

Specimen		Maximum load	Number of fibers			Maximum load per
Series	No.	P_{max} (kN)	Top side	Bottom side	Total	fiber $P_{ind.max}$ [N]
Fc48-1%	1	13.25	101	97	198	66.91
	2	12.82	105	86	191	67.13
	3	11.80	92	94	186	63.44
	4	11.97	97	101	198	60.46
	5	13.33	107	99	206	64.72
Fc48-1% (α=11.2)	Cal.	7.25	$=V_f \cdot A_m / A_f \cdot \eta_f$ $=0.01\times(60\times70)/0.196\times0.544$		116.6	62.320
Fc48-2%	2	18.28	156	148	304	60.14
	3	17.27	163	144	307	56.25
	4	15.53	131	149	280	55.46
Fc48-2% (α=9.1)	Cal.	13.32	$=V_f \cdot A_m / A_f \cdot \eta_f$ $=0.02\times(60\times70)/0.196\times0.544$		233.1	57.248

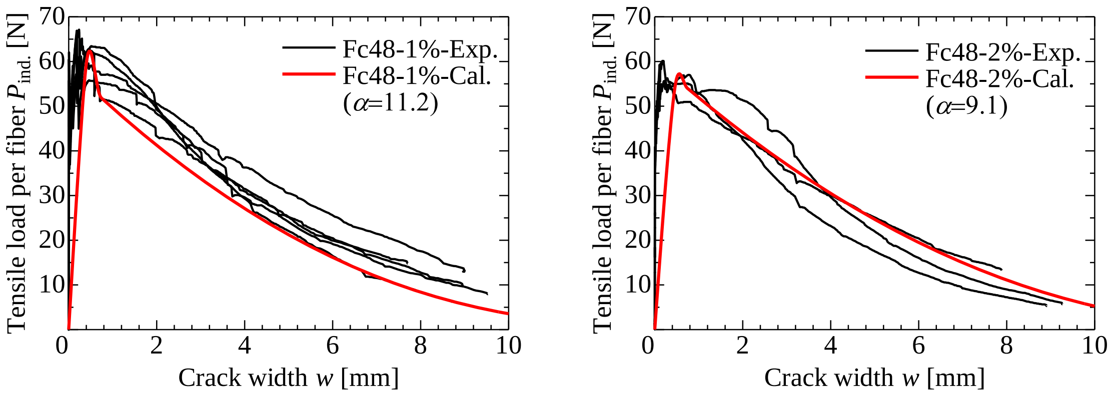

Figure 3.1 (iii) Tensile load per fiber $P_{ind.}$ - crack width w relationship (Fc48)

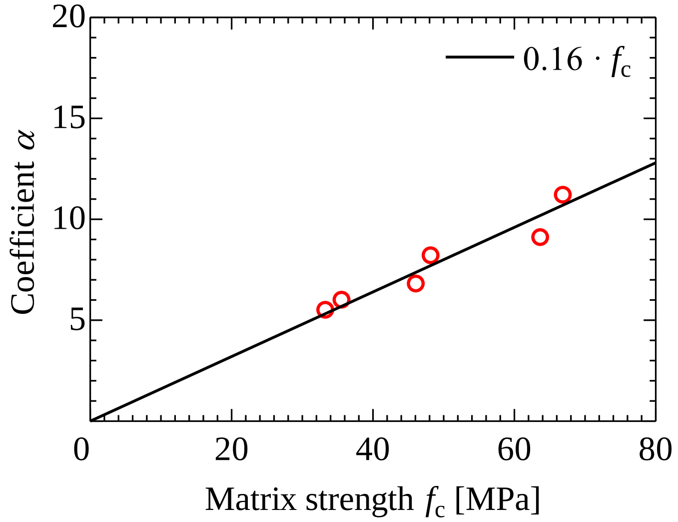

Figure 3.2 Relationship between coefficient α and matrix strength f_c

3.3 Modeling of Bridging Law

The calculated bridging law, in which matrix strength f_c is set to be 45MPa, for the orientation intensity k ranging from 0.1 to 10 are shown in **Figure 3.3**. In order to simply express the elliptic distribution, orientation intensity k, which is the average value of k_{xy} and k_{zx}, is applied in the modeling. The bridging laws shown in the figure are calculated with 0.1 intervals of k in the case of $k < 1$, and with 1 interval when $k > 1$. The parameters adopted for the calculation are set the same as those in **Table 3.1**, excepting fiber orientation intensity k. The coefficient α are calculated by the relational expression with matrix strength f_c, as given by Equation (2). In addition, volume fraction of fibers is set to be 2%. As revealed by the results, bridging stress σ_{bridge} decreases gradually after peak, and becomes 0 when crack width reaches to 15mm (half of fiber length) because most of the fibers are completely pulled out from the matrix. On the other hand, by comparing each curve, the maximum bridging stress remarkably increases with the increase of orientation intensity k, which means that bridging stress σ_{bridge} becomes larger when the fibers strongly orient to the normal direction of the crack surface.

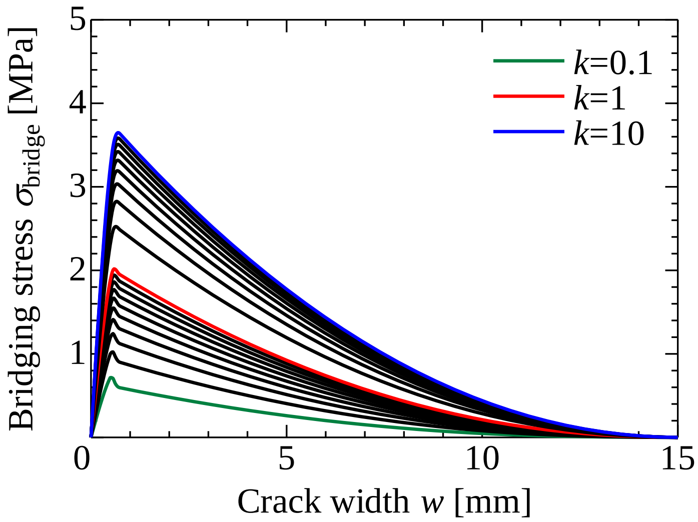

Figure 3.3 Calculation results of bridging law (f_c = 45MPa)

The calculated bridging laws are modeled by simple forms considering fiber orientation and matrix strength, to utilize them effectively in various types of structural elements. As shown in **Figure 3.4**, bridging law is simply characterized by two regions: the curve until the maximum stress and softening branch, so the bridging law is simplified to a bilinear model. The bilinear model has three parameters: the maximum bridging stress σ_{max}, the crack width at maximum bridging stress w_{max}, and the crack width when bridging stress reach 0 w_{tu}. The values of σ_{max} and w_{max} of the model can be obtained directly from the calculation results. The value of w_{tu} is determined to have an equivalent fracture energy with the calculated bridging law in the softening branch. The modeled bridging law, in which matrix strength f_c is set to be 45MPa, for the orientation intensity k ranging from 0.1 to 10 are shown in **Figure 3.5**.

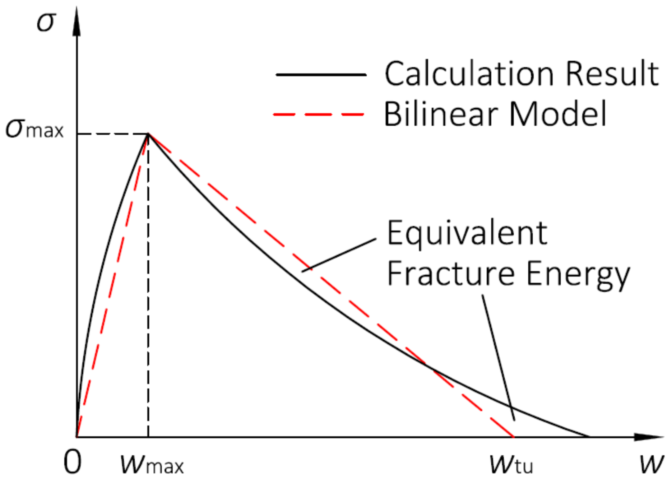

Figure 3.4 Bilinear model for bridging law

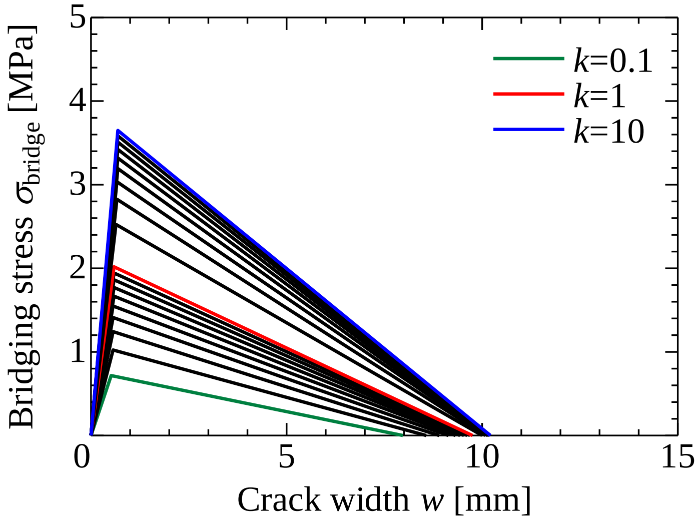

Figure 3.5 Modeled bridging law (f_c = 45MPa)

Figure 3.6 shows the relationship between each parameter of bilinear model and orientation intensity k (f_c = 45MPa). The black line in each figure exhibits the modified regression calculation results by the least square method, to simplify the relational expression between each parameter and fiber orientation intensity k. In order to take the influence of matrix strength into consideration, it is assumed that each parameter can be expressed as the functions given by Equations (3) to (5). Coefficients A to E in the equations are considered to be affected by matrix strength f_c.

$$\sigma_{max} = A \cdot k^{B} \quad [\text{MPa}] \tag{3}$$

$$w_{max} = C \cdot k^{D} \quad [\text{mm}] \tag{4}$$

$$w_{tu} = E \cdot k^{F} \quad [\text{mm}] \tag{5}$$

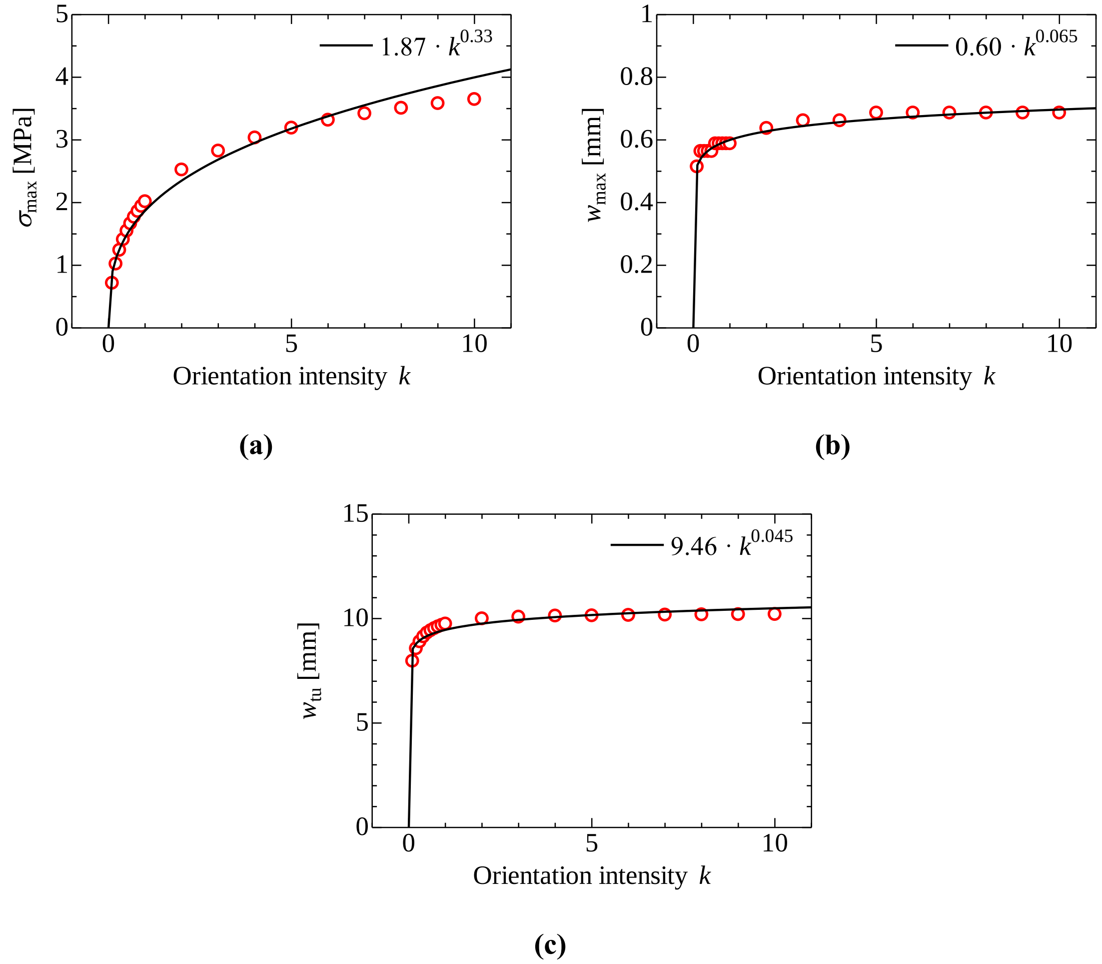

Figure 3.6 Relationship between each parameter and orientation intensity k (f_c = 45MPa): (a) Maximum bridging stress σ_{max}; (b) Crack width at maximum bridging stress w_{max}; (c) Crack width when bridging stress reach 0 w_{tu}

The same calculations are conducted with 5MPa intervals of matrix strength f_c in the case of 20MPa to 60MPa, as shown in **Figure 3.7**. According to the calculation for each matrix strength f_c, coefficients A to E can be obtained from the modified regression calculation results of each parameter, as shown in **Figure 3.8**. **Table 3.3** shows the coefficients of parameters for bilinear model in each matrix strength f_c. However, when matrix strength f_c is smaller than 30MPa, the calculation results of k ranging from 0.1 to 10 do not show any rupture of fibers, as shown in **Figure 3.8** and **Figure 3.9**. Consequently, w_{max} and w_{tu} do not change obviously with the change of fiber orientation intensity k, as shown in **Figure 3.8**. Therefore, when matrix strength f_c is smaller than 30MPa, the values of w_{max} and w_{tu} are obtained from the average values of calculation results.

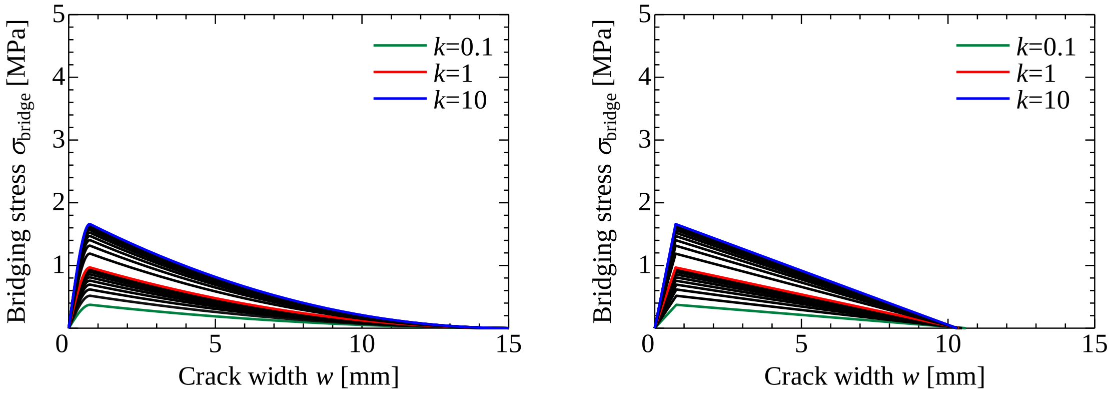

(a) (b)

Figure 3.7 (i) Calculated and modeled bridging law (f_c = 20MPa)
(a) Calculation results; (b) Modeled bridging law

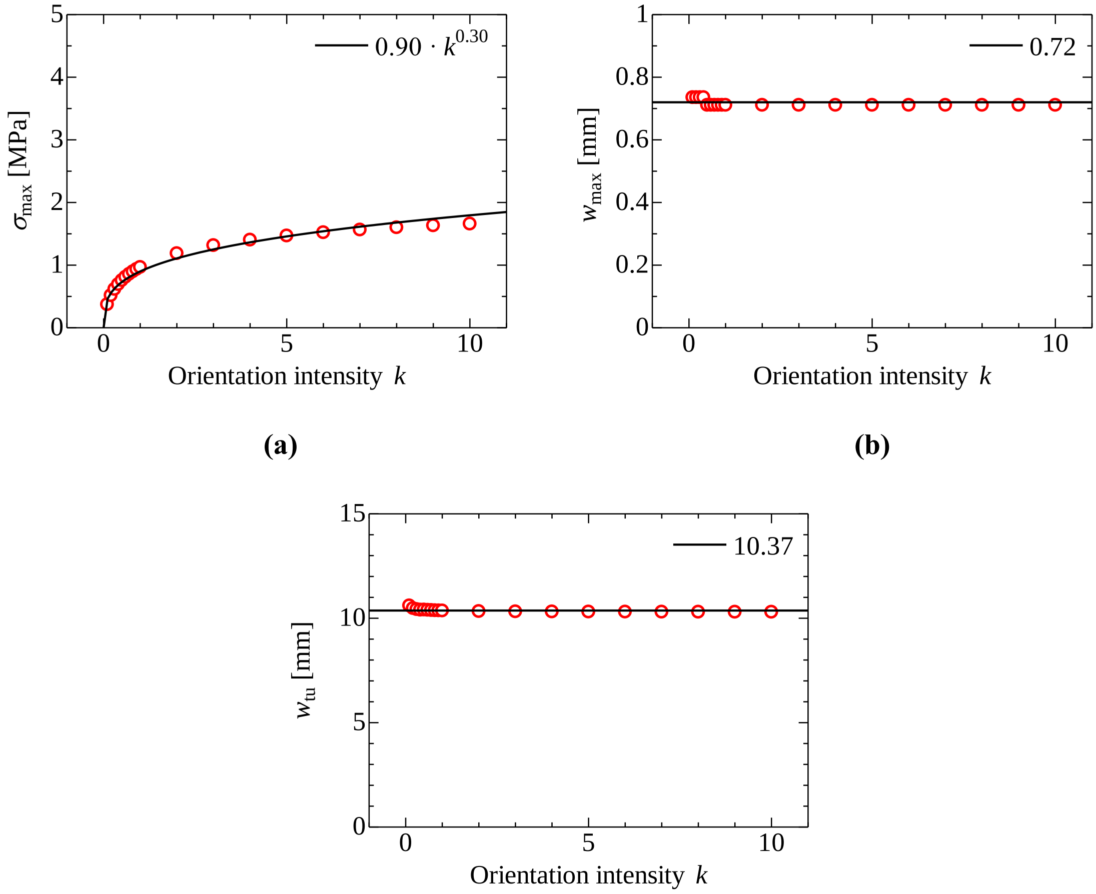

(a) (b)

(c)

Figure 3.8 (i) Relationship between each parameter and orientation intensity *k* (f_c = 20MPa):
(a) Maximum bridging stress σ_{max}; (b) Crack width at maximum bridging stress w_{max};
(c) Crack width when bridging stress reach 0 w_{tu}

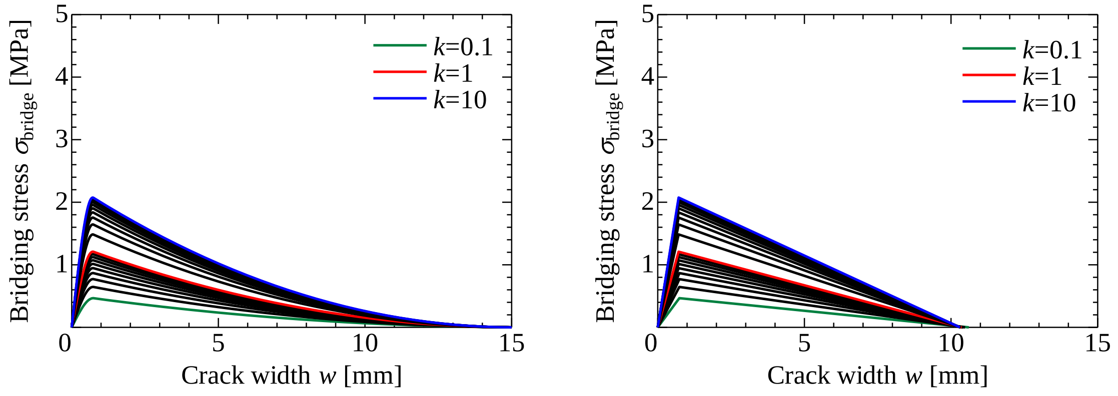

(a) **(b)**

Figure 3.7 (ii) Calculated and modeled bridging law (f_c = 25MPa)

(a) Calculation results; (b) Modeled bridging law

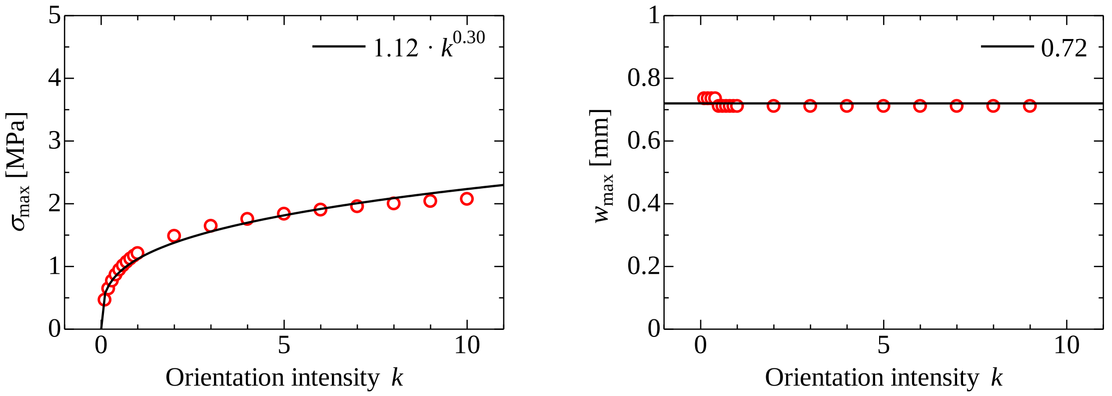

(a) **(b)**

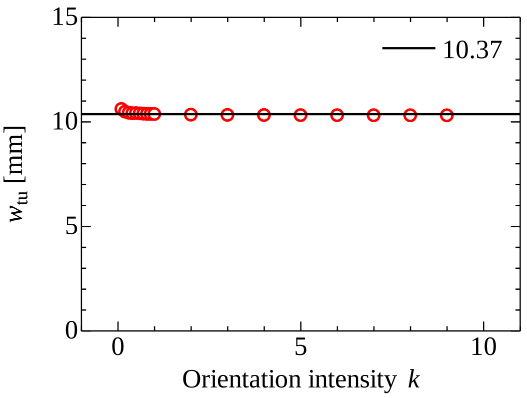

(c)

Figure 3.8 (ii) Relationship between each parameter and orientation intensity *k* (f_c = 25MPa):

(a) Maximum bridging stress σ_{max}; (b) Crack width at maximum bridging stress w_{max};

(c) Crack width when bridging stress reach 0 w_{tu}

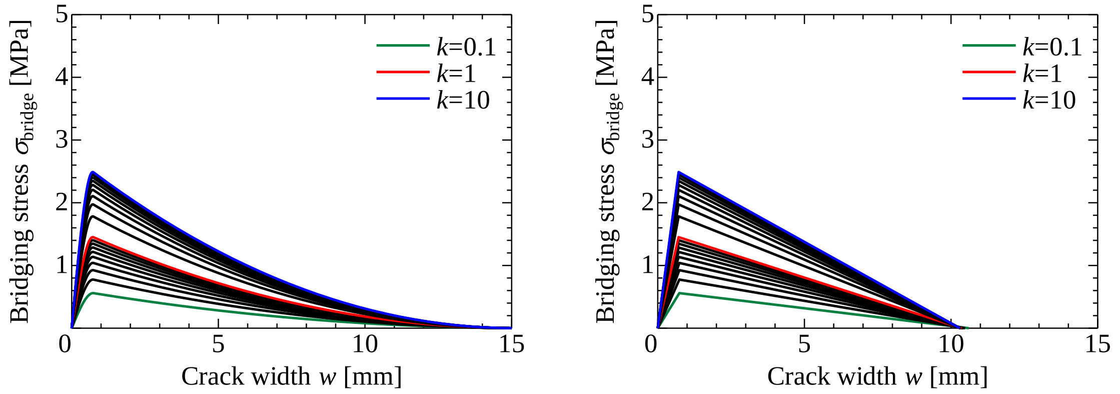

(a) **(b)**

Figure 3.7 (iii) Calculated and modeled bridging law (f_c = 30MPa)

(a) Calculation results; (b) Modeled bridging law

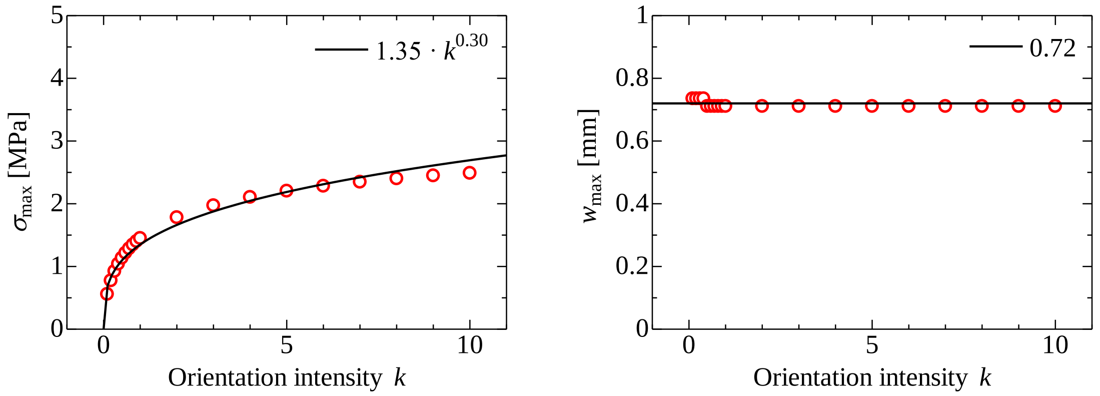

(a) **(b)**

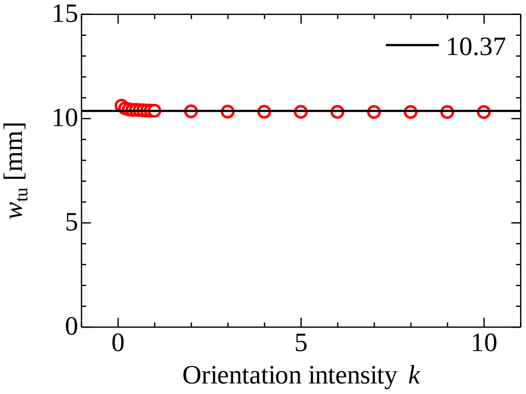

(c)

Figure 3.8 (iii) Relationship between each parameter and orientation intensity *k* (f_c = 30MPa):

(a) Maximum bridging stress σ_{max}; (b) Crack width at maximum bridging stress w_{max};

(c) Crack width when bridging stress reach 0 w_{tu}

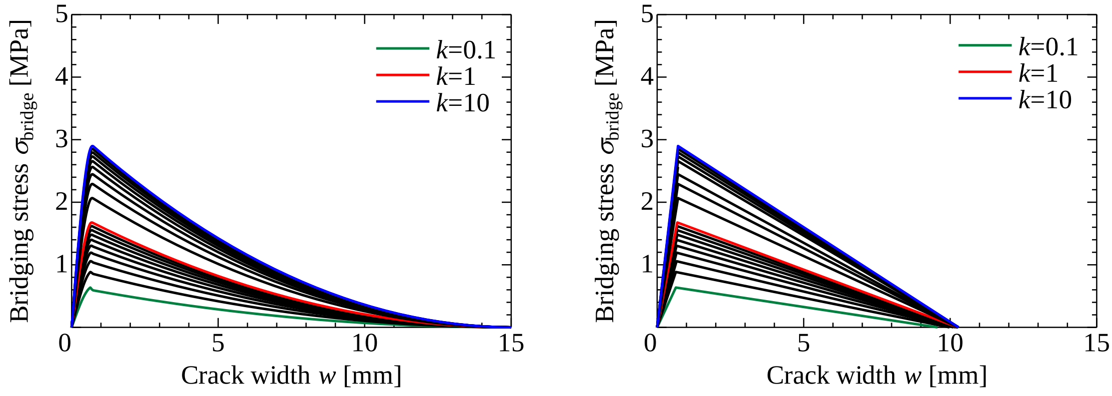

(a) **(b)**

Figure 3.7 (iv) Calculated and modeled bridging law (f_c = 35MPa)
(a) Calculation results; (b) Modeled bridging law

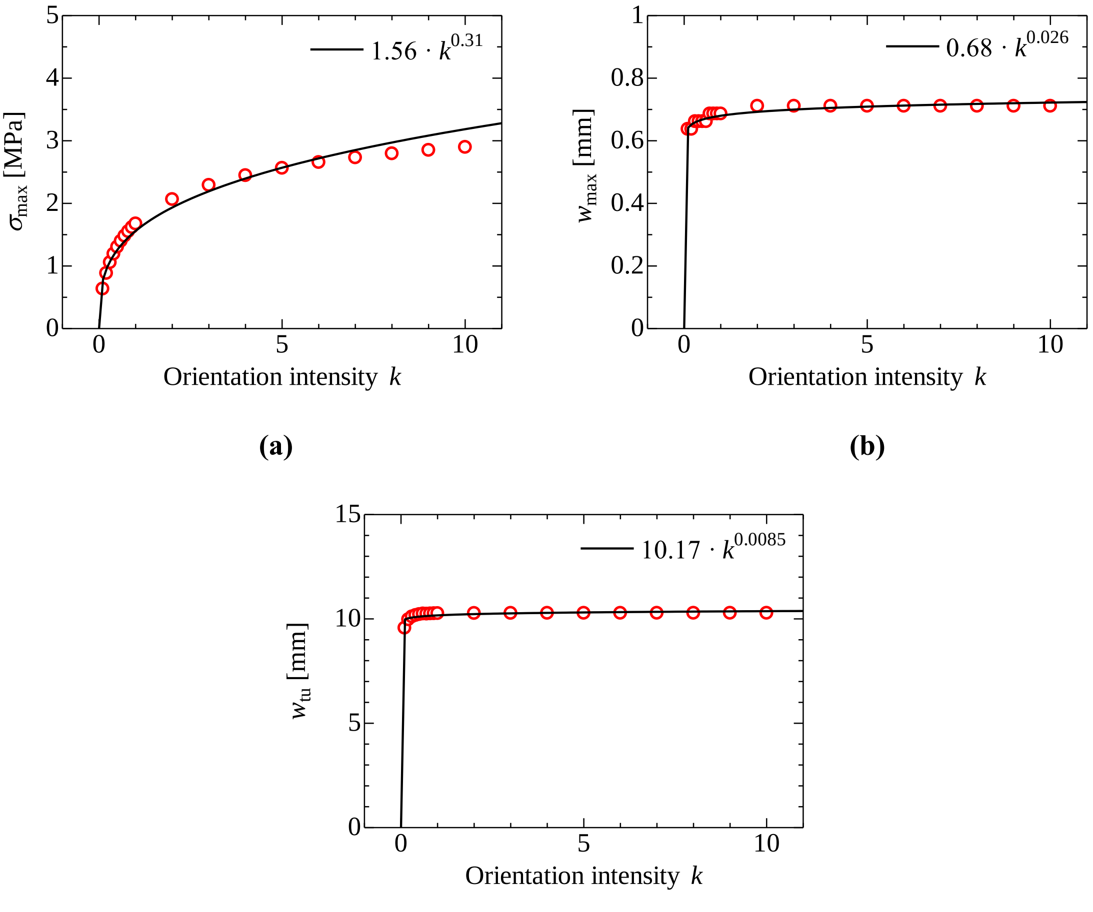

(a) **(b)** **(c)**

Figure 3.8 (iv) Relationship between each parameter and orientation intensity k (f_c = 35MPa):
(a) Maximum bridging stress σ_{max}; (b) Crack width at maximum bridging stress w_{max};
(c) Crack width when bridging stress reach 0 w_{tu}

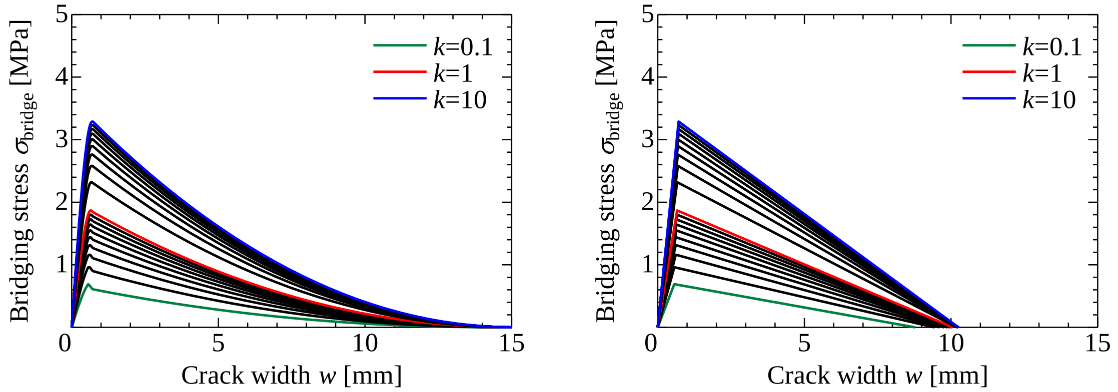

(a) **(b)**

Figure 3.7 (v) Calculated and modeled bridging law (f_c = 40MPa)
(a) Calculation results; (b) Modeled bridging law

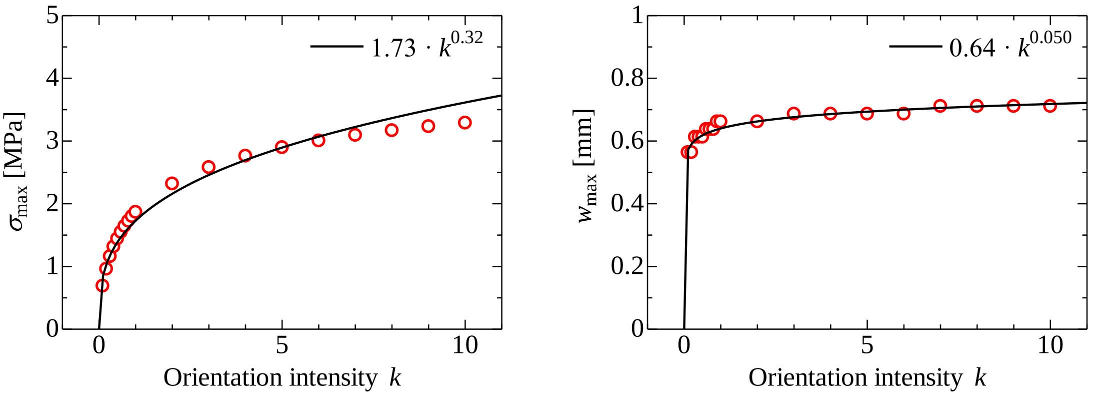

(a) **(b)**

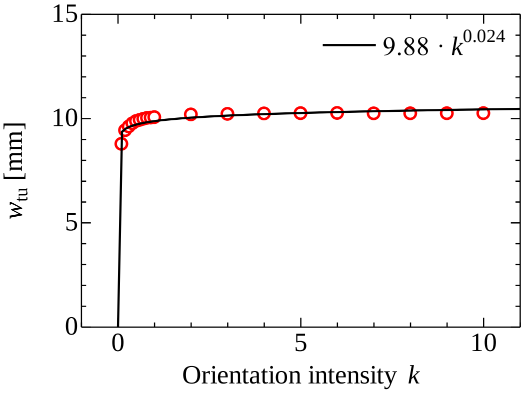

(c)

Figure 3.8 (v) Relationship between each parameter and orientation intensity k (f_c = 40MPa):
(a) Maximum bridging stress σ_{max}; (b) Crack width at maximum bridging stress w_{max};
(c) Crack width when bridging stress reach 0 w_{tu}

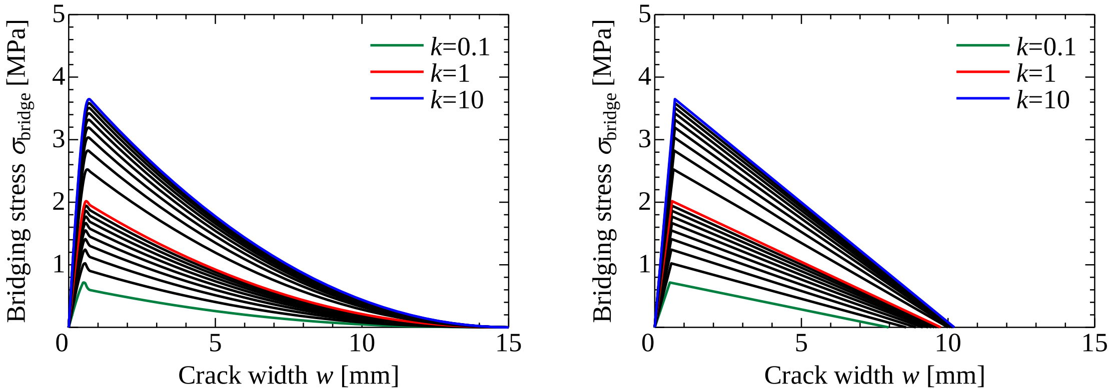

(a) **(b)**

Figure 3.7 (vi) Calculated and modeled bridging law (f_c = 45MPa)

(a) Calculation results; (b) Modeled bridging law

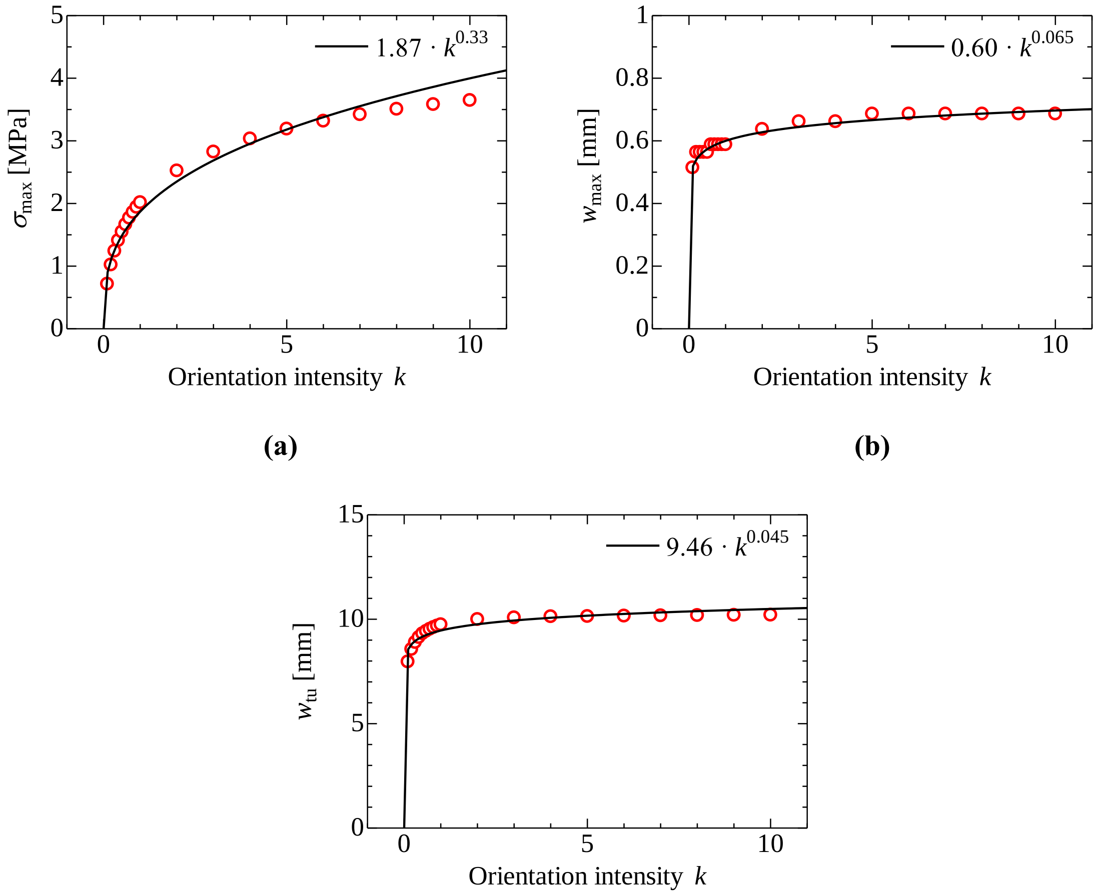

(a) **(b)**

(c)

Figure 3.8 (vi) Relationship between each parameter and orientation intensity *k* (f_c = 45MPa): (a) Maximum bridging stress σ_{max}; (b) Crack width at maximum bridging stress w_{max}; (c) Crack width when bridging stress reach 0 w_{tu}

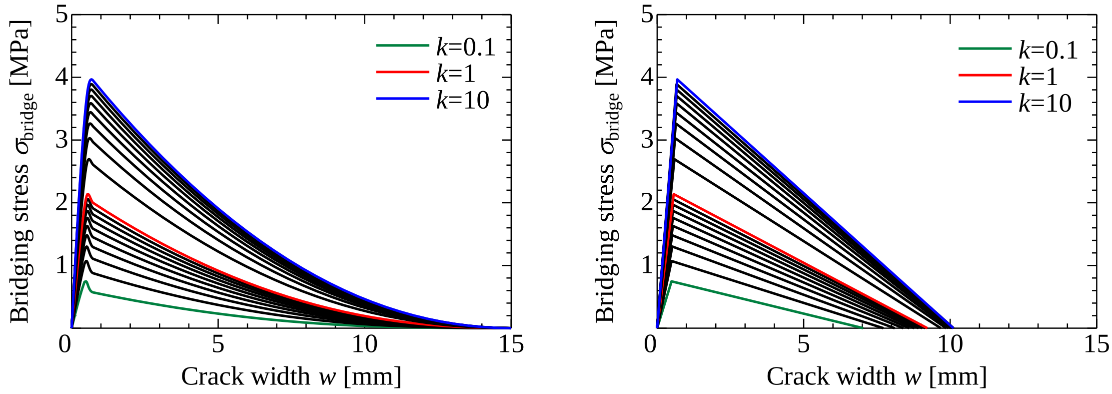

(a) **(b)**

Figure 3.7 (vii) Calculated and modeled bridging law (f_c = 50MPa)
(a) Calculation results; (b) Modeled bridging law

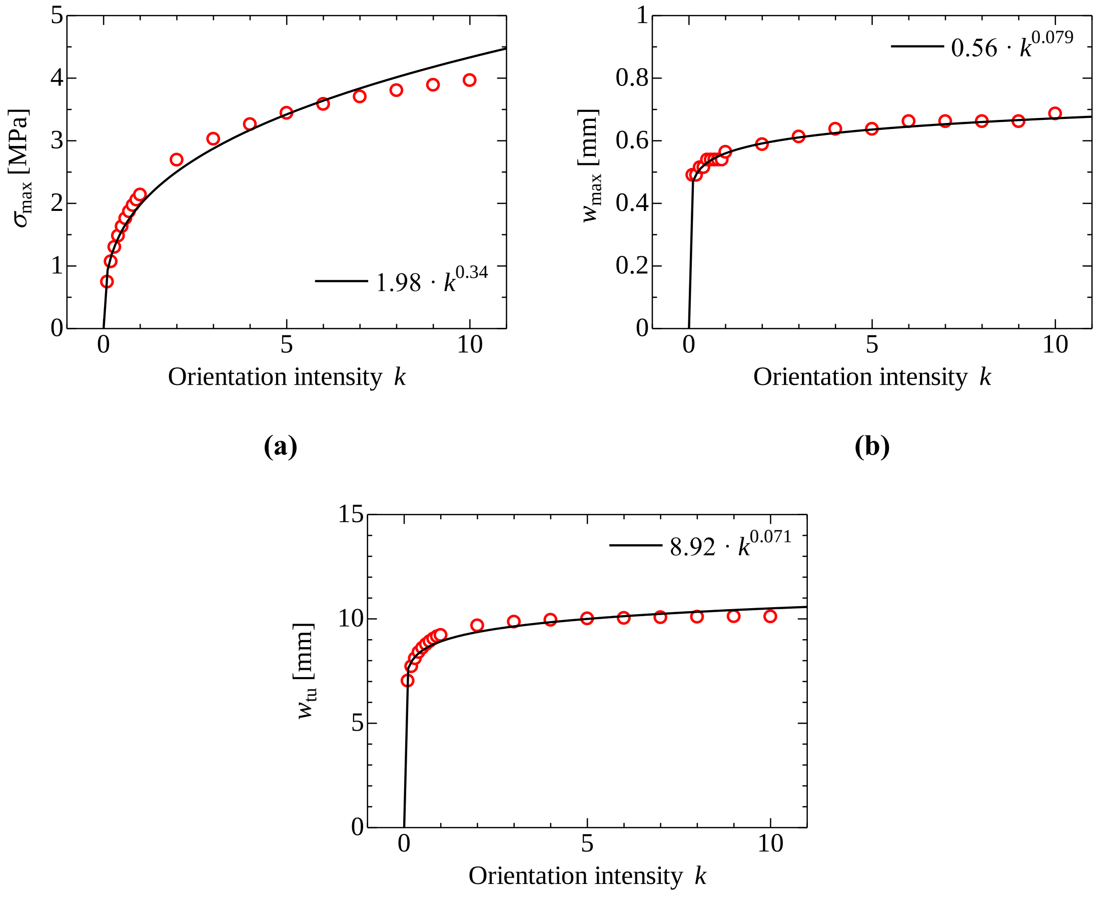

(c)

Figure 3.8 (vii) Relationship between each parameter and orientation intensity *k* (f_c = 50MPa):
(a) Maximum bridging stress σ_{max}; (b) Crack width at maximum bridging stress w_{max};
(c) Crack width when bridging stress reach 0 w_{tu}

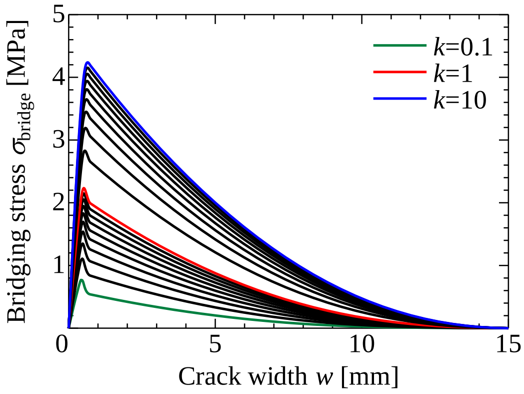

(a)

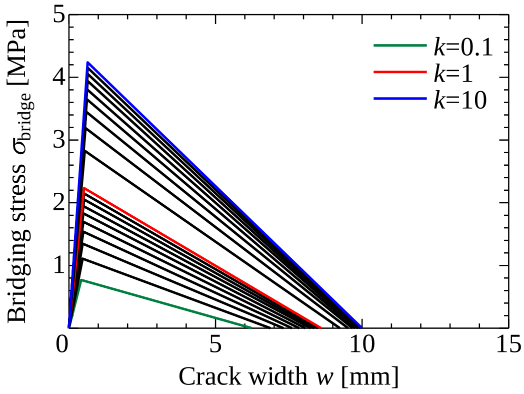

(b)

Figure 3.7 (viii) Calculated and modeled bridging law (f_c = 55MPa)

(a) Calculation results; (b) Modeled bridging law

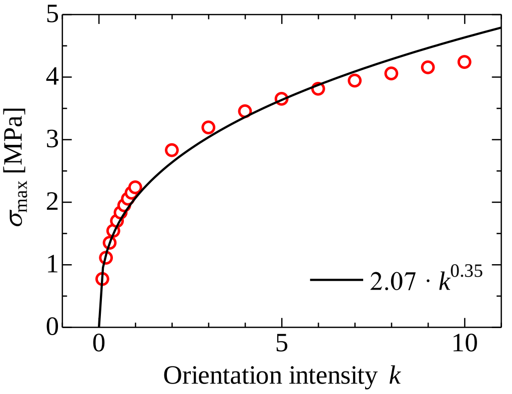

(a)

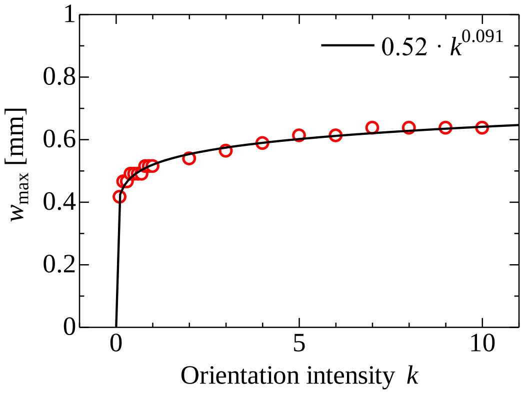

(b)

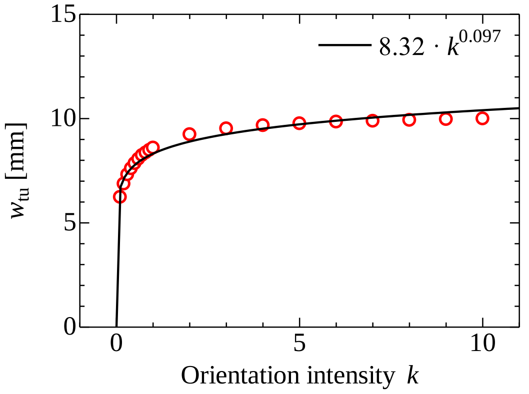

(c)

Figure 3.8 (viii) Relationship between each parameter and orientation intensity *k* (f_c = 55MPa):

(a) Maximum bridging stress σ_{max}; (b) Crack width at maximum bridging stress w_{max};

(c) Crack width when bridging stress reach 0 w_{tu}

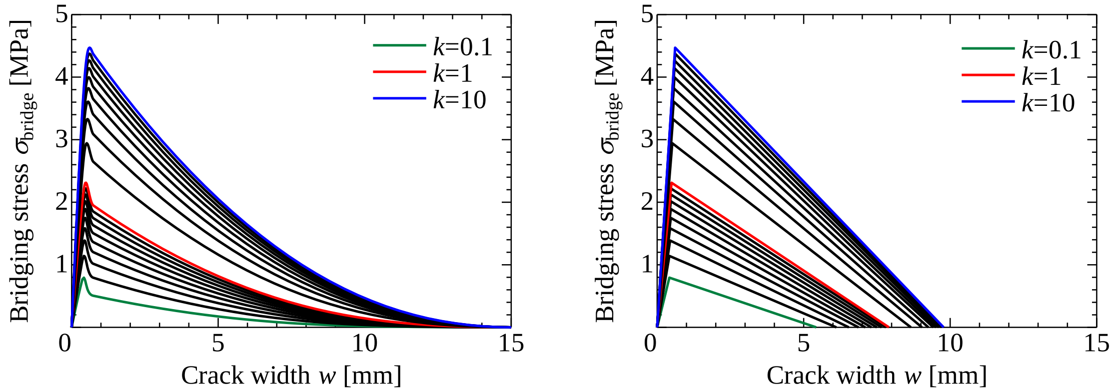

(a) **(b)**

Figure 3.7 (ix) Calculated and modeled bridging law (f_c = 60MPa)
(a) Calculation results; (b) Modeled bridging law

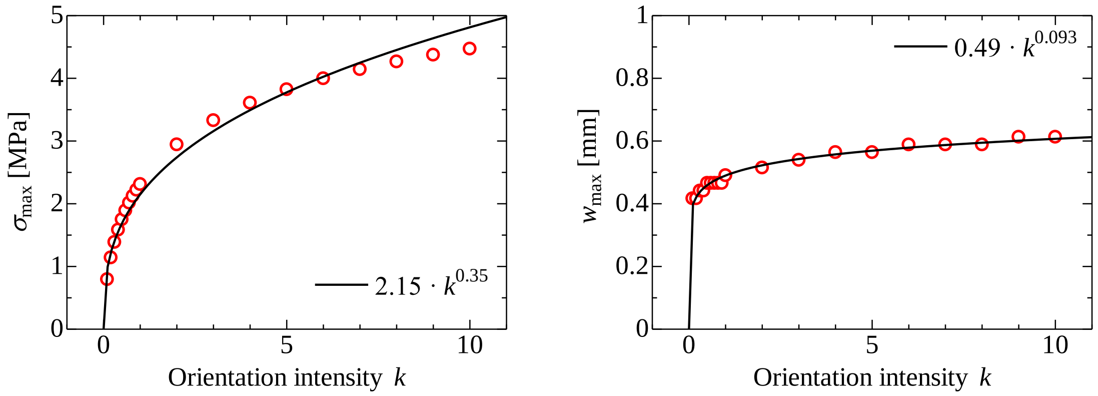

(a) **(b)**

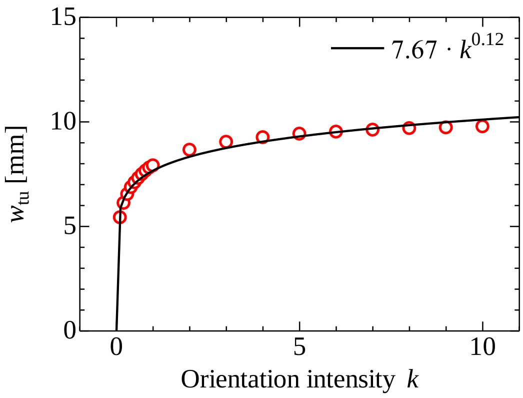

(c)

Figure 3.8 (ix) Relationship between each parameter and orientation intensity *k* (f_c = 60MPa):
(a) Maximum bridging stress σ_{max}; (b) Crack width at maximum bridging stress w_{max};
(c) Crack width when bridging stress reach 0 w_{tu}

Table 3.3 Coefficients of parameters for bilinear model

Matrix strength f_c [MPa]	Coefficients of parameters for bilinear model					
	A	B	C	D	E	F
20	0.90	0.30	0.72*	0	10.37*	0
25	1.12	0.30	0.72*	0	10.37*	0
30	1.35	0.30	0.72*	0	10.37*	0
35	1.56	0.31	0.68	0.026	10.17	0.0085
40	1.73	0.32	0.64	0.050	9.88	0.024
45	1.87	0.33	0.60	0.065	9.46	0.045
50	1.98	0.34	0.56	0.079	8.92	0.071
55	2.07	0.35	0.52	0.091	8.32	0.097
60	2.15	0.35	0.49	0.093	7.67	0.12

* Obtained by the average values of calculation results

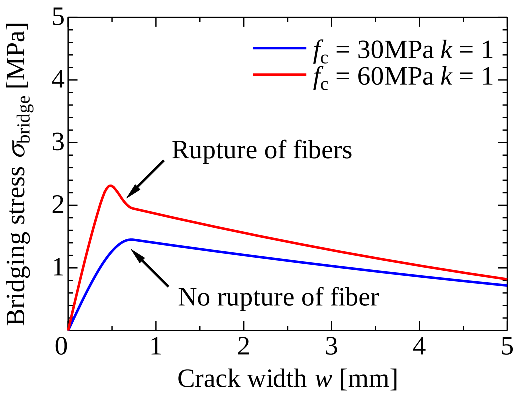

(a)

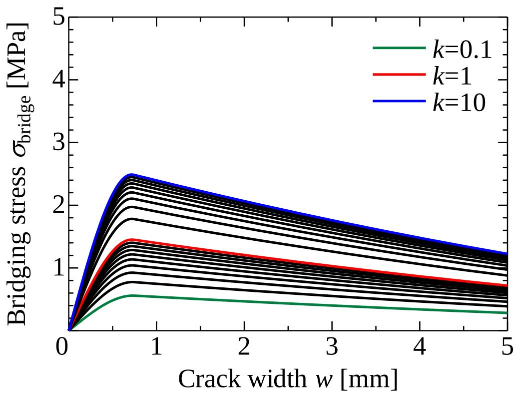

(b)

Figure 3.9 Calculation results of bridging law ($f_c \leq$ 30MPa)

(a) Bridging law showing rupture of fibers or not; (b) Calculated bridging law (f_c = 30MPa)

Figure 3.10 shows the relationship between each coefficient and matrix strength f_c. The black line in each figure exhibits the modified regression calculation results by the least square method, to simplify the relational expression between each coefficient and matrix strength f_c. In the case of coefficient B to F, the solid lines exhibit the modified regression calculation results when f_c is larger than 30MPa, while dotted lines exhibit the ones when f_c is smaller than 30MPa. The relational expression between each coefficient and matrix strength f_c is given by Equations (6) to (11).

$$A = 0.087 \cdot f_c^{0.80} \quad f_c \in [20, 60] \tag{6}$$

$$B = \begin{cases} 0.30 & f_c \in [20, 30] \\ 0.13 \cdot f_c^{0.24} & f_c \in (30, 60] \end{cases} \tag{7}$$

$$C = \begin{cases} 0.72 & f_c \in [20, 30] \\ 0.95 - 0.0078 \cdot f_c & f_c \in (30, 60] \end{cases} \tag{8}$$

$$D = \begin{cases} 0 & f_c \in [20, 30] \\ 0.19 - 5.82 / f_c & f_c \in (30, 60] \end{cases} \tag{9}$$

$$E = \begin{cases} 10.37 & f_c \in [20, 30] \\ 9.65 + 0.082 \cdot f_c - 0.0019 \cdot f_c^2 & f_c \in (30, 60] \end{cases} \tag{10}$$

$$F = \begin{cases} 0 & f_c \in [20, 30] \\ -0.012 - 0.0016 \cdot f_c + 0.000064 \cdot f_c^2 & f_c \in (30, 60] \end{cases} \tag{11}$$

where,

unit for matrix strength f_c is MPa.

The feature points of bilinear model of bridging law in each fiber orientation intensity k and matrix strength f_c, can be easily obtained using Equations (3) to (11).

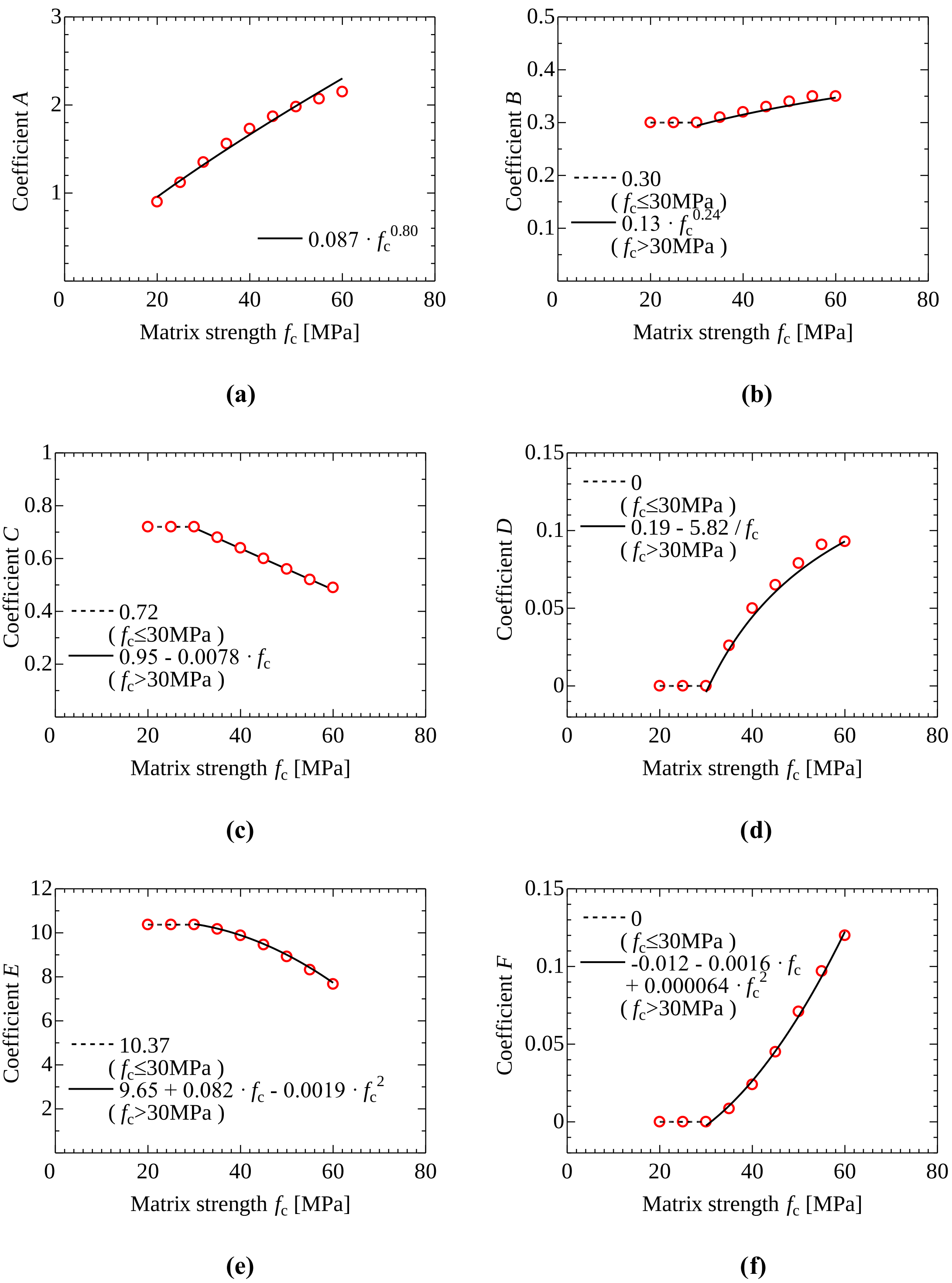

Figure 3.10 Relationship between each coefficient and matrix strength f_c
(a) Coefficient A; (b) Coefficient B; (c) Coefficient C;
(d) Coefficient D; (e) Coefficient E; (f) Coefficient F

3.4 Adaptability of Modeled Bridging Law

3.4.1 4-point Bending Test

4-point bending test is conducted for DFRCC specimens to investigate the bending performance experimentally. Bending specimens are rectangular prisms of 100×100×400mm. The applied materials are the same as those described in Section **2.2.2**. For each series, five bending specimens were manufactured and cured in the natural environment.

4-point bending test was carried out using a universal testing machine of 2MN capacity. Image of 4-point bending test is shown in **Figure 3.11**. Load was applied to the specimen on the trisection points of span, and loading speed was set to be 0.5mm/min. Two displacement transducers (Pi-type) were set at the compression and tension sides of constant bending moment area with a vertical distance of 70mm. Measurement items were load P, axial deformation of compression side δ_1 and axial deformation of tension side δ_2. Bending moment M and curvature φ can be calculated by Equations (12) to (13) and bending moment M - curvature φ relationship can be obtained.

$$M = \frac{P}{2} \cdot \frac{L}{3} \quad [\mathrm{kN \cdot m}] \tag{12}$$

$$\varphi = \frac{\varepsilon_2 - \varepsilon_1}{d_0} \quad [1/\mathrm{m}] \tag{13}$$

where,

P = load applied to specimen,

L = span (= 300mm),

ε_1, ε_2 = strain obtained from dividing deformation δ_1 and δ_2 by 100mm (gauge length)

d_0 = vertical distance between two displacement transducers (= 70mm)

The bending specimens, in which the localized crack opened out of the constant bending moment area, are not discussed in the following parts.

Before 4-point bending test, compressive test was also conducted to confirm the compressive strength and elastic modulus. For each series, three cylinder specimens (φ100 × 200mm) were tested. **Table 3.4** shows the compressive properties of each series. As revealed by the results, compressive strength of the three mix proportions showed obvious difference to each other. In addition, by comparing with results shown in **Table 2.4**, compressive strength increased remarkedly with increasing of curing time.

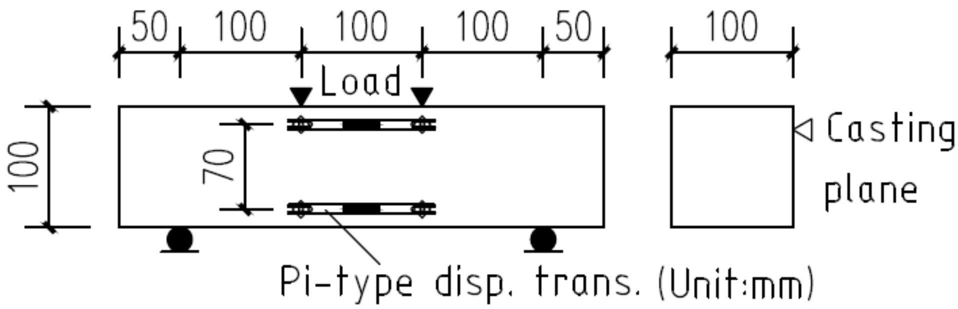

Figure 3.11 Image of 4-point bending test

Table 3.4 Compressive properties (4-point bending test)

Series	Fiber volume fraction [%]	Curing time [Days]	Compressive strength [MPa]	Elastic modulus [GPa]
Fc24	None	6	26.6	11.2
	1		24.4	11.2
	2		24.0	10.7
Fc36	None	8	37.1	14.9
	1		34.8	15.2
	2		35.1	14.5
Fc48	None	11	52.6	17.4
	1		53.7	17.8
	2		53.0	17.0

3.4.2 Section Analysis

In order to verify the adaptability of the modeled bridging law proposed in Section **3.3**, the section analysis under bending condition based on the modeled bridging law is conducted.

Figure 3.12 shows the stress σ - strain ε model applied in section analysis. As for compression side, a parabola model based on the experimental results of compressive test is used. As for tension side, the trilinear model consists of two parts: elastic part and bridging law part. Feature point of elastic part is obtained based on experimental results, which parameters can be calculated by Equations (14) to (15). Feature points of bridging law part are obtained from the bilinear model of bridging law proposed in Section **3.3**, which parameters can be calculated by Equations (16) to (18). **Table 3.5** shows the parameters for the model applied in section analysis of each series. The fiber orientation intensity k is set to be 3.8, which refers to previous study [12]. Matrix strength f_c is obtained from the compressive test results of cylinder specimens manufactured in the same batch of bending specimens. As for the series of 1% fibers, it is assumed that stress σ in bridging law part is half of that of 2% fibers.

$$\sigma_{cr} = \frac{M_{cr}}{Z} = \frac{6 \cdot M_{cr}}{b \cdot h^2} \quad [\mathrm{MPa}] \tag{14}$$

$$\varepsilon_{cr} = \frac{\sigma_{cr}}{E_c} \tag{15}$$

where,

M_{cr} = bending moment when the first crack generates (obtained from 4-point bending test),

Z = section modulus (= $b \cdot h^2/6$),

b, h = dimensions of cross-section,

E_c = elastic modulus (obtained from compressive test).

$$\sigma_t = \sigma_{max} \quad [\mathrm{MPa}] \tag{16}$$

$$\varepsilon_t = \frac{w_{max}}{l_t} \tag{17}$$

$$\varepsilon_u = \frac{w_{tu}}{l_t} \tag{18}$$

where,

σ_{max}, w_{max}, w_{tu} = parameters of bilinear model of bridging law (Equation (3) to (5)),

l_t = length of constant bending moment area of 4-point bending test (= 100mm).

The section analysis is conducted based on the assumption that cross-section remains plain when considering its deformation. Firstly, curvature φ is given. After that, the strain ε of each element in cross-section is calculated from linear distribution of strain and stress for each element is obtained from the stress σ - strain ε model shown in **Figure 3.12**. Finally, neutral axis satisfying equilibrium condition is found numerically and bending moment M can be calculated. When calculations are conducted for curvature φ from 0 to 0.8 (unit: 1/m) with fine intervals, analyzed bending moment M - curvature φ relationships can be obtained.

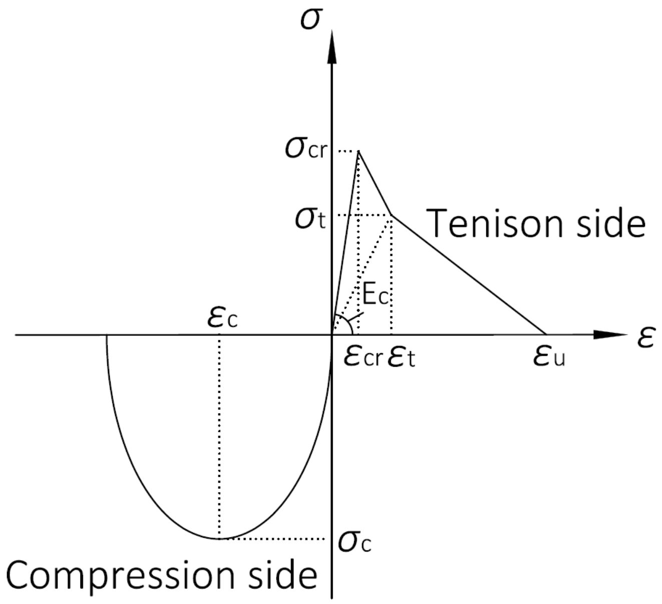

Figure 3.12 Stress σ - strain ε model applied in section analysis

Table 3.5 Parameters for stress σ - strain ε model applied in section analysis

Series	f_c [MPa]	k	Compression side		Tension side				
					Elastic part		Bridging law part		
			σ_c [MPa]	ε_c	σ_{cr} [MPa]	ε_{cr}	σ_t [MPa]	ε_t	ε_u
Fc24-1%	24.4	3.8	-24.4	-0.005	2.136	0.00019	0.836	0.0072	0.104
Fc24-2%	24.0		-24.0		2.604	0.00024	1.651	0.0072	0.104
Fc36-1%	34.8		-34.8		2.772	0.00018	1.118	0.0070	0.103
Fc36-2%	35.1		-35.1		2.982	0.00021	2.253	0.0070	0.103
Fc48-1%	53.7		-53.7		2.946	0.00016	1.654	0.0059	0.096
Fc48-2%	53.0		-53.0		3.432	0.00020	3.269	0.0060	0.097

3.4.3 Comparison of Analysis and Experimental Results

Figure 3.13 shows the bending moment M - curvature φ relationship, in which black lines exhibit the experimental results obtained from 4-point bending test, while red lines exhibit the analysis results. According to the observation after loading, the number of cracks in constant bending moment area of DFRCC specimens did not show obvious difference with the change of fiber volume fraction. **Table 3.6** shows the maximum bending moment M_{max} of experimental and analysis results for each series. As revealed in **Figure 3.13**, analysis results show good agreements with experimental results in the series of 2% fiber volume fraction. As for the series of 1% fiber volume fraction, the difference of the shape of post-peak branch is considered to be due to the number and distribution of fibers across the fracture surface. As shown in **Table 3.6**, maximum bending moment M_{max} of experimental results is from 0.910 to 1.105 times of that of analysis results.

Table 3.6 Maximum bending moment M_{max} of experimental and analysis results

Series	Maximum bending moment M_{max} [kN·m]		Exp. / Ana.
	Exp.*	Ana.	
Fc24-1%	0.714	0.723	0.988
Fc24-2%	0.925	0.906	1.021
Fc36-1%	1.048	0.948	1.105
Fc36-2%	1.207	1.104	1.093
Fc48-1%	1.051	1.065	0.987
Fc48-2%	1.303	1.432	0.910

* Average value of experimental results

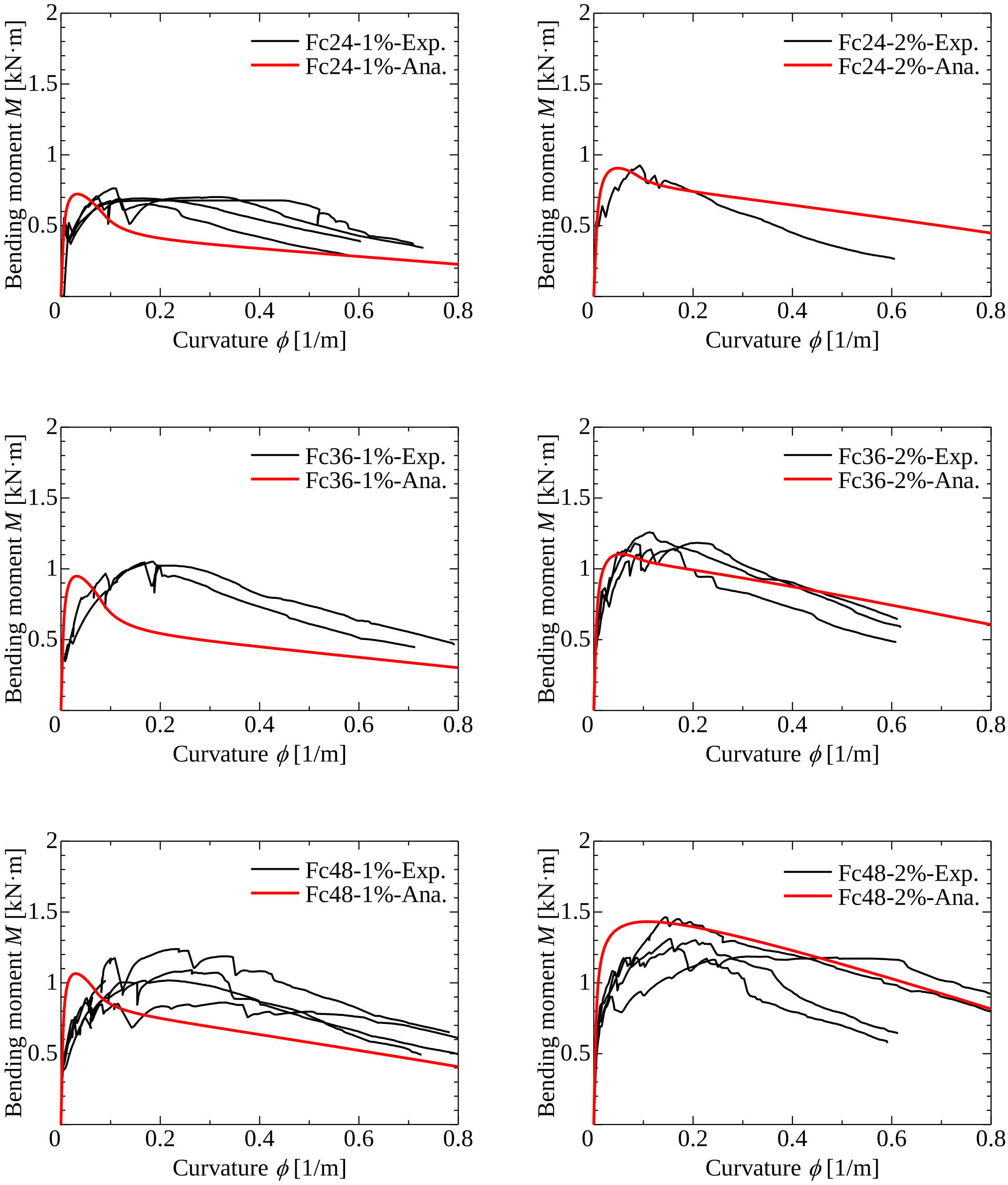

Figure 3.13 Bending moment M - curvature φ relationship

Chapter 4 Conclusion

This study investigated the influence of matrix strength on the tensile performance of DFRCC with bundled aramid fibers. A total of 45 specimens varying matrix strength and fiber volume fraction were subjected to uniaxial tension test. Based on the experimental and calculation results, bridging law model, in which feature points were expressed by the function of fiber orientation intensity and matrix strength was proposed. Adaptability of the modeled bridging law was verified through section analysis for 4-point bending test. The main conclusions of this study are summarized as follows.

(1) In uniaxial tension test, according to the observation after loading, most of the DFRCC specimens in tensile failure showed multiple cracks. Number of cracks increased with increasing of matrix strength. The load at first cracking and the maximum load also increased with increasing of matrix strength.

(2) From the results of the calculation of bridging law, the modified individual fiber pullout model, in which the maximum pullout force is given by the proportional relations with the compressive strength of matrix, could express the uniaxial tension test results well.

(3) The calculated bridging law using the modified fiber pullout model was simplified to a bilinear model, in which feature points were expressed by the function of fiber orientation intensity and matrix strength.

(4) Section analysis under bending condition was conducted for series with different matrix strength and fiber volume fraction using the modeled bridging law. The maximum bending moment of experimental results was from 0.910 to 1.105 times of that of analysis results.

Acknowledgements

First of all, please allow me to express my sincerest appreciation to my academic supervisor, Prof. Toshiyuki Kanakubo, for his precious guidance, constructive supervision, priceless feedback, and pleasant communication during this research project. Without his encouragement and support, this thesis could not be completed. His extensive research experience and keen insight have impressed me deeply and will certainly encourage me for the rest of my life.

I would also like to convey my appreciation to my vice-academic supervisor Associate Prof. Akira Yasojima and a technical staff member Mr. Kojima, for their extremely important assistance on my experiment and their valuable comments on my research project.

In addition, I would like to thank all the members in this laboratory for their kind support and creating such a nice working environment. Special thanks go to Mr. Daiki Sunaga, Mr. Takumi Koba, and Mr. Jin Wang for their help in executing experimental works.

Finally, special thanks are also expressed to my dearest parents for their endless love and continuous support in my life.

Reference

[1] Matsumoto, T., Mihashi, H.: JCI-DFRCC Summary Report on DFRCC Terminologies and Application Concepts, Proceedings of the JCI International Workshop on Ductile Fiber Reinforced Cementitious Composites (DFRCC), 2002

[2] 佐野直哉，八十島章，山田大，金久保利之：接合部に DFRCC を用いた PCa 柱梁接合部の構造性能，コンクリート工学年次論文集，Vol.37, No.2, 2015.7

[3] 丸田誠，閑田徹志，永井覚，山本幸正：プレキャス ECC 連結梁を用いた高層 RC 新架構，コンクリート工学，Vol.43, No.11, 2005

[4] 日本コンクリート工学会：繊維補強セメント複合材料の新しい利用法研究委員会報告書，2012.9

[5] Uchida, Y., Takeyama, T., Dei, T.: Ultra high strength fiber reinforced concrete using aramid fiber, Proceedings of the 7th International Conference on Fracture Mechanics of Concrete and Concrete Structures, Jeju, Korea, 2010.5

[6] Pitcha, J., Chung, N.T., Ganchai, T., Linh, V.H. Bui.: Mechanical properties of aramid fiber-reinforced composites and performance on repairing concrete beams damaged by corrosion, Songklanakarin J. Sci. Technol 42, 2020

[7] Kiyota, M., Mihashi, H., Kanda, T., Kawamata, A.: Study on Bond Characteristics of Fibers in Cementitious Composites, Proceedings of the Japan Concrete Institute, Sapporo, Hokkaido, Japan, Volume 23, No.2, 2001.7

[8] Wang, Y., Backer, S., Li, V.C.: A statistical tensile model of fiber reinforced cementitious composites, Composites 1989, 20, 1989

[9] Shannag, M., Brincker, R., Hansen, W.: Pullout behavior of steel fibers from cement-based composites, Cem. Concr. Res, 1997

[10] Kanakubo, T., Echizen, S., Wang, J., Mu, Y.: Pullout Behavior of Bundled Aramid Fiber in Fiber-Reinforced Cementitious Composite, Materials, Vol.13, No.7, 1746, 2020

[11] Wang, Y., et al..: Analysis of Synthetic Fiber Pull-Out from a Cement Matrix, MRS Proc, 1987

[12] Kanakubo, T., et al.: Influence of Fiber Orientation on Bridging Performance of Polyvinyl Alcohol Fiber-Reinforced Cementitious Composites, ACI Mater. J. 2016

[13] Kanakubo, T., Miyaguchi, M., Asano, K.: Influence of Fiber Orientation on Bridging Performance of Polyvinyl Alcohol Fiber-Reinforced Cementitious Composite, Materials Journal, American Concrete Institute, Vol.113, No.2, 2016

[14] Ozu, Y., Miyaguchi, M. Kanakubo, T.: Modeling of Bridging Law for PVA Fiber-Reinforced Cementitious Composites Considering Fiber Orientation, Journal of Civil Engineering and Architecture 12, 2018

[15] Sunaga, D., Koba, T., Kanakubo, T.: Modeling of Bridging Law for Bundled Aramid Fiber-Reinforced Cementitious Composite and its Adaptability in Crack Width Evaluation, Materials, Vol.14, No.1, 179, 2021

[16] Li, Jiayue., Deng, Zongcai.: Tensile Behavior of Hybrid Fiber-Reinforced Ultra-High-Performance Concrete, front. Mater., 2021

[17] Seung Hun Park, et al.: Tensile Behavior of Ultra High Performance Hybrid Reinforced Concrete, Cement & Concrete Composites 34, 2012